Journal of Infrared, Millimeter, and Terahertz Waves (2023) 44:169–211
https://doi.org/10.1007/s10762-022-00902-1

INVITED REVIEW ARTICLE

Terahertz Beam Steering: from Fundamentals to Applications

Yasuaki Monnai[1] · **Xuyang Lu**[2] · **Kaushik Sengupta**[3]

Received: 18 July 2022 / Accepted: 26 December 2022 / Published online: 20 February 2023

Abstract

Free-space transmission of terahertz (THz) waves opens great opportunities for wireless applications including sensing and communication in the 6G era and beyond. Owing to their wider bandwidths and shorter wavelengths, the use of THz waves enhances information capacity and spatial resolution while downsizing aperture sizes compared to microwaves. On the other hand, the shorter wavelengths of THz waves can involve severe path loss. To compensate for the path loss, directional transmission based on beam steering is indispensable. In this article, we review the development of THz beam steering, which has been a longstanding challenge as well as the generation of high-power THz waves. While the use of active or passive phased arrays is the predominantly utilized approach to implement beam steering, other approaches based on variable diffractive structures and frequency dispersive structures offer low-cost alternatives. We also emphasize that application-driven system design approaches, in which THz beam steering is tightly coupled to signal processing, have been emerging to overcome hardware limitations.

Keywords Terahertz · Beam steering · Phased arrays · Phase shifters · Diffraction gratings · Distributed index lenses · Leaky-wave antennas

1 Introduction

Wireless transmission of signals in the frequency range of 0.1–1 THz, i.e., the terahertz (THz) band, has been vigorously studied for a variety of applications including nondestructive imaging, high-resolution radar, and communication in the 6G era and

✉ Yasuaki Monnai
monnai@star.rcast.u-tokyo.ac.jp

[1] Research Center for Advanced Science and Technology, The University of Tokyo, Tokyo, Japan

[2] University of Michigan - Shanghai Jiao Tong University Joint Institute, Shanghai, China

[3] Department of Electrical and Computer Engineering, Princeton University, Princeton, NJ, USA

beyond. Owing to the typically wider bandwidths available in this spectrum and shorter wavelengths, the use of THz waves enhances information capacity and spatial resolution while requiring lower physical apertures (for the same gain) than at microwave frequencies. Even for short-range transmission of an order of 1 m, the propagation distance is much longer than the THz wavelengths, which for 300 GHz is 1 mm. Therefore, compensation for the path loss using a highly directional link is essential. In general, the path loss between a transmitter and a receiver (with polarization alignment) is described based on the Friis transmission formula [1] as

$$\frac{P_r}{P_t} = \left(\frac{\lambda}{4\pi R}\right)^2 g_t g_r, \tag{1}$$

where P_t and P_r are the transmitted and received power, respectively, λ is the wavelength, and R is the distance between the transmitter and receiver, each with a linear antenna gain of g_t and g_r, respectively. From Eq. 1, we see that the path loss is proportional to the square of λ and increases significantly as the wavelength becomes shorter. Thus, large g_t and g_r are required to compensate for the path loss. When we assume $R = 10^n\lambda$ and express the antenna gain in decibels using capital letters G_t and G_r, the path loss in Eq. 1 is expressed as $20n + 22 - G_t - G_r$ dB. For example, the path loss becomes 22 dB when $n = 3$ and $G_t = G_r = 30$ dB ($g_t = g_r = 1000$). It should be mentioned here that the wireless transmission of THz waves also suffers from atmospheric attenuation. Nevertheless, it can be minimized by the use of atmospheric windows at which the attenuation becomes a few decibels per kilometer around 300 GHz [2]. Therefore, the path loss likely far exceeds the atmospheric attenuation when the propagation distance is sub-kilometer. While the Friis transmission formula in Eq. 1 describes the path loss with respect to line-of-sight transmission, non-line-of-sight transmission is also important in practical situations. In that case, additional reflection losses are involved.

Increasing antenna gains requires two technical considerations in size and alignment. Firstly, a large antenna aperture is needed because the antenna gain g is proportional to its aperture area A_e as [1]

$$g = \frac{4\pi A_e}{\lambda^2}. \tag{2}$$

To implement large A_e, a feeding structure that uniformly excites the large aperture must be realized. An aperture with large A_e can deliver a collimated beam over a certain distance. We can see that if we assume $P_r/P_t = 1$ and $g_t = g_r = g$ in Eq. 1, and when combined with Eq. 2, we obtain $R = A_e/\lambda$. This relation provides an estimate of the distance over which beam collimation is maintained without wavefront divergence. Also, according to the definition of the antenna gain, the following relation holds

$$g = \frac{4\pi}{\Theta_1 \Theta_2}, \tag{3}$$

where Θ_1 and Θ_2 are the two orthogonal beamwidths in the azimuth and elevation directions in radians. As a numerical example, when we prepare a uniform aperture of 30 mm square ($A_e = 900$ mm^2) for $\lambda = 1$ mm, we can generate a beam collimated over a distance of about 0.9 m, and the beam begins to diverge after that with a

beamwidth of about 2°. In many experimental studies in the THz range, horn antennas and lenses are frequently used to implement such a large aperture. To excite such a large aperture with a point source, wavefront conversion using a tapered waveguide or free-space diffraction is required. Since axial propagation is involved for the conversion, increasing the aperture area without increasing its three-dimensional volume is difficult. In the microwave range, techniques to implement a large aperture with a low-profile have been developed such as patch antenna arrays. However, applying such techniques directly to the THz range is challenging due to significant losses of transmission lines comprising both conductive and dielectric losses. Hence, beamforming techniques that can circumvent the significant losses in the THz range need to be developed [3].

Secondly, dynamic beam steering is required to extend the spatial coverage of signal transmission [4]. In the THz range, diffraction towards the shadow region behind objects hardly occurs since the wavelength is much shorter than that of microwaves. Therefore, transmitters and receivers must be linked via adaptively selected line-of-sight and non-line-of-sight paths using beam steering. In the microwave range, phased arrays have been established as a technique for beam steering, in which a wavefront is artificially synthesized by an array of antennas with individually controlled phases [1]. Phased arrays can be broadly classified into active and passive types as illustrated in Fig. 1(a) and (b), respectively. In the active type, each oscillation phase of multiple oscillators is controlled individually, whereas, in the passive type, the output of a single oscillator is distributed to multiple antennas via phase shifters. In either case, the gain of a single antenna is multiplied by an array factor described as

$$F(\hat{\boldsymbol{r}}) = a_0 e^{j(k_0 \hat{\boldsymbol{r}} \cdot \boldsymbol{d}_0 + \Delta\phi_0)} + a_1 e^{j(k_0 \hat{\boldsymbol{r}} \cdot \boldsymbol{d}_1 + \Delta\phi_1)} + \cdots + a_{N-1} e^{j(k_0 \hat{\boldsymbol{r}} \cdot \boldsymbol{d}_{N-1} + \Delta\phi_{N-1})} \quad (4)$$

where $F(\hat{\boldsymbol{r}})$ denotes the array factor formed in the direction of a unit vector $\hat{\boldsymbol{r}}$, k_0 is the wavenumber in free-space, and a_n, $\boldsymbol{d}_n$, and $\Delta\phi_n$ are the amplitude, displacement vector, and phase delay of the n-th element, respectively. When the amplitude a_n is uniform and the phase delay is chosen so that $\Delta\phi_n = k_0 \hat{\boldsymbol{r}}_0 \cdot (\boldsymbol{d}_0 - \boldsymbol{d}_n) + \Delta\phi_0 + 2\pi m$ holds, where m is an integer, constructive interference is established in the specific direction of $\hat{\boldsymbol{r}}_0$. The grating lobes can be suppressed when the array is dense enough, i.e., $-\pi < k_0 \hat{\boldsymbol{r}} \cdot (\boldsymbol{d}_n - \boldsymbol{d}_{n-1}) < \pi$. Thus, beam steering can be attained by dynamically tuning the values of $\Delta\phi_n$. With N antenna elements, the array factor enhances the gain of a single antenna by a factor of N when mutual coupling between adjacent elements is negligible. For example, when an isotropic antenna element with a gain of $g = 4\pi A/\lambda^2 = 1$ is arrayed with $N = 16$, the total gain becomes 12 dB. Other beam shapes including focused beams and multi-directional beams can also be synthesized by accordingly tuning the phase.

In the following sections, we review the recent development of THz beam steering with an emphasis on fundamental challenges and application possibilities. Currently, research and development of semiconductor transmitters and receivers in the THz range are being vigorously pursued [5, 6]. Accordingly, important results on THz phased arrays have been reported as reviewed in Section 2. Meanwhile, there are significant challenges in implementing large-scale phased arrays mainly due to the lack of transmission lines and phase shifters that are sufficiently low-loss and broadband.

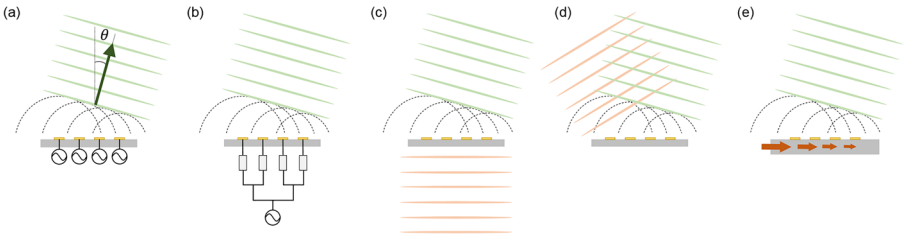

Fig. 1 **a** Active phased array. **b** Passive phased array. **c** Parallel-fed diffraction with a transmissive array. **d** Parallel-fed diffraction with a reflectarray. **e** Serial-fed diffraction with a leaky-wave antenna

Therefore, alternative approaches have also been considered based on reconfigurable diffraction using variable structures as reviewed in Section 3 and frequency dispersive structures in Section 4. Such approaches are classified into transmission-type, reflection-type, and also guided-type (Fig. 1(c), (d), and (e)) although their beam patterns can be commonly described by the array factor in Eq. 4. In addition to the efforts as above, we emphasize in Section 5 that application-driven approaches have recently been emerging. There, beam steering with dispersive structures can be used for physical layer signal processing such as spectrum-to-space mapping, implementing functionality with limited hardware resources.

2 Phased Arrays

In this section, we start with reviewing the recent development of THz phased arrays. Whether active or passive, electronic or optical, the phased arrays incorporate multiple antenna elements to emulate a large aperture antenna with the capability of directing the beam into specific directions (Fig. 1(a) and (b)). The enhancement of antenna gain using the phased arrays is important for not only transmitters but also receivers as understood from Eq. 1.

2.1 Overview of the THz Generation Methods

As shown in Fig. 2(a), candidates of THz power generation at the low THz frequencies mainly include silicon technologies such as complementary metal-oxide semiconductors (CMOS), SiGe, III-IV semiconductor-based heterojunction bipolar transistors (HBTs), high electron mobility transistors (HEMTs), Schottky barrier diodes (SBDs), resonant tunneling diodes (RTDs), and quantum cascaded lasers (QCLs) [5]. For every technology, the reported THz power generation has shown significant evolution from 2008 to 2018 as summarized in Fig. 2(b). Transistor-based methods are advantageous at the low THz frequencies owing to their efficiency and compatibility with well-developed CMOS processes for large-scale integration. For

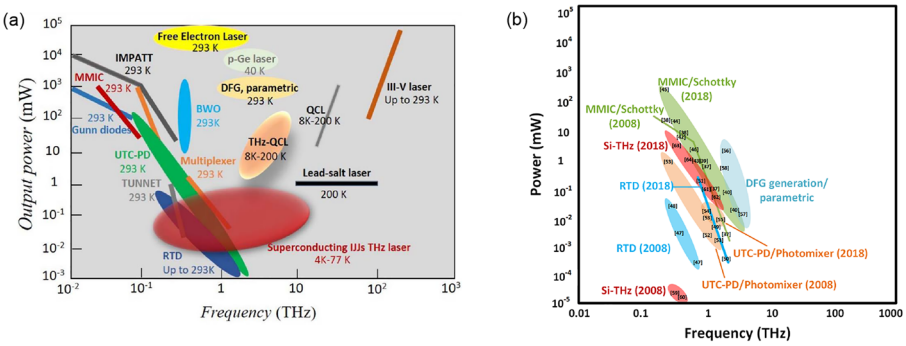

Fig. 2 **a** General trends of THz power generation across different technological substrates and frequency ranges [7]. Copyright 2020, IEEE. **b** Evolution of the reported THz power generation in integrated electronics and photonic systems from 2008 to 2018 [5]. Copyright 2018, Springer Nature

transistor-based THz power generation, a Johnson's figure of merit serves as a performance metric. Another indicator for high-frequency operation is the maximum frequency of operation ($f_{\max}$), which is the frequency where the unilateral gain becomes unity. This limit is determined by several different device parameters including intrinsic gain, on-chip metal losses at terminals, parasitic capacitance, breakdown voltage, and carrier mobility. As an example, an InP/GaAsSb double heterojunction bipolar transistor (DHBT) with an $f_{\max}$ of 1.2 THz has been reported [8]. For general CMOS/SiGe technologies, an $f_{\max}$ close to 250/500 GHz can be expected. Additional losses attributed to on-chip passive devices could also reduce the efficiency of high-frequency operation. Silicon-based THz sources above 300 GHz were first demonstrated in 2008 by Huang et al. [9] and Seok et al. [10]. The first THz beam-scanning array operating at 280 GHz was demonstrated in CMOS with +9.4 dBm effective isotropic radiated power (EIRP) in [11–13]. Since then, the community has made significant advancements (as shown in Fig. 2(b)) with THz frequency generation in CMOS stretching up to 1.4 THz (at −13 dBm EIRP) [14]. In [15], a 1-THz oscillator array was demonstrated with an EIRP of 13 dBm and a DC-to-RF efficiency of 0.73×10^{-4}. The efficiency and $f_{\max}$ of silicon-based devices, particularly SiGe, is expected to increase as the fabrication processes improve. As an example, to enhance the total radiated power and directivity, a non-tunable 2D array for power combining has been developed to deliver 1 mW of radiated power at 0.53 THz, where synchronization between antenna elements is realized with a zigzag daisy chain [16]. Beam steering has gained increasing attention also for other THz generation methods such as RTDs and QCLs. RTDs have shown oscillation frequency close to 2 THz at room temperature [17]. Phase control of an injection locked RTD at around 380 GHz has been investigated with an aim for array extension [18]. QCLs typically show higher efficiencies at higher frequencies, but it requires operation at low temperatures. An efficiency of 2% has been reported at 3.3 THz at 70 K [19]. Phase

locking of QCLs has been considered through serially connected laser ridges [20] and evanescent coupling [21].

2.2 Active Phased Arrays

To enable intelligent THz sensing and communication in the 6G era and beyond, the adoption of phased arrays is in the middle of the spotlight owing to its beamforming capability in the spatial domain. One of the critical challenges in realizing large-scale arrays is the signal distribution and synchronization between array elements for coherent power combining. As illustrated in Fig. 3(a) and (b), popular methods for synchronization include an H-tree distribution network of a local oscillator (LO) signal and an array of mutually coupled oscillators. Examples of the respective methods are shown in Fig. 3(c) [11] and (d) [22]. The H-tree distribution network consists of a fractal tree structure typically fabricated with transmission lines. As a result, the LO signal reaching every cell has an equal amount of delay, resulting in a uniform frequency, amplitude, and phase. Each cell can contain a frequency multiplier and a phase shifter so that the radiation wavefront can be tilted. A drawback in this method is that the LO signal is severely attenuated on the network and needs to be compensated by broadband amplifiers. This comes at a cost of complexity, high DC power consumption, and potential mismatches due to process variations. Furthermore, the presence of a dense LO network can involve unintentional wave coupling that deteriorates the radiation performance. Meanwhile, in the coupled oscillator network as shown in Fig. 3(b), adjacent oscillators connected in a mesh are mutually locked. This approach significantly simplifies the design of the coupling network, but the phase tuning range in the coupled oscillators is typically limited by the phase-locking range of the oscillators. It should be noted that while the abovementioned array architectures are useful as a transmitter, it is significantly more challenging to use them as a receiver.

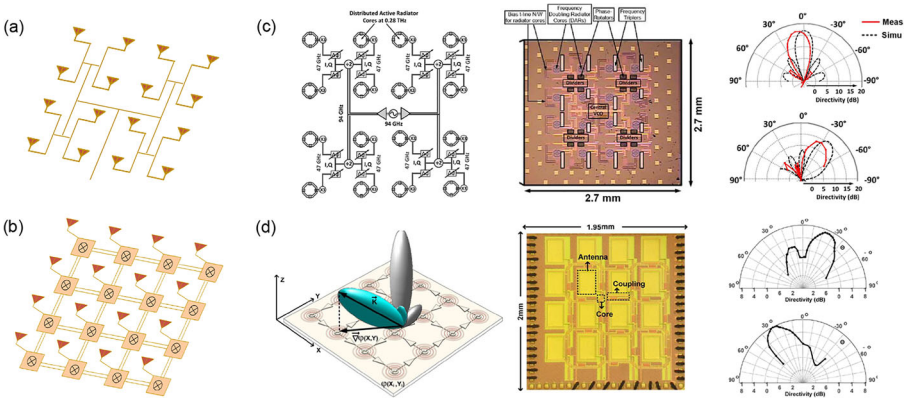

Fig. 3 Array synchronization strategies using **a** H-tree distribution network and **b** coupled oscillator network. **c** Example of an H-tree based phased array at 280 GHz [11]. Copyright 2012, IEEE. **d** Example of a coupled oscillator–based phased array at 338 GHz [22]. Copyright 2015, IEEE

An H-tree LO distribution network requires phase shifting for each radiator. Such phase shifting can be in principle implemented with vector-sum phase shifters consisting of two variable gain amplifiers. However, its implementation at THz frequencies is challenging due to the absence of amplifier gain. Thus, several other phase-shifting schemes have been proposed including RF/LO phase shifting, intermediate frequency phase-shifting, and digital phase-shifting in fully digital arrays. Digital arrays, while being the most flexible and programmable in their operation, require a full transceiver chain and an ADC at each element. Minimizing power consumption of the digitizers operating at high-speed for practical, efficient, and scalable digital array architectures is an ongoing research challenge. The challenge of intermediate frequency (IF) is that the spatial interferers are not rejected before the frequency down-conversion and the inter-modulation products can be detrimental to the array operation. Li et al. proposed a 140-GHz phased array transmitter based on a scheme with high IF phase-shifting where an IF frequency of 11.5 GHz is used, and the IQ phase component is generated through a polyphase filter [23] (Fig. 4(a)). Abdo et al. demonstrated an image-rejection transceiver operating at 300 GHz through bi-directional outphasing and Hartley architecture as shown in Fig. 4(b). The work achieves a TX and an RX data rate of 26 Gbaud and 18 Gbaud, respectively [24].

For coupled oscillator arrays, beamforming is typically realized by changing the bias voltage of the oscillators so that the relative phase of the injection current and the oscillation current is shifted, that in turn changes the phase of the oscillator relative to the neighboring element. This implies a strong tuning range dependence on the locking range of coupled oscillators. A locking range of approximately 8 GHz was reported at 200 GHz using a mutual coupling array [26, 27]. Another implementation of a mutually coupled resonator network can be found in [22], where each of the cells is locked to its neighbors through transmission line–based coupling networks with varactors. Any phase tuning at the fundamental frequency gets directly translated

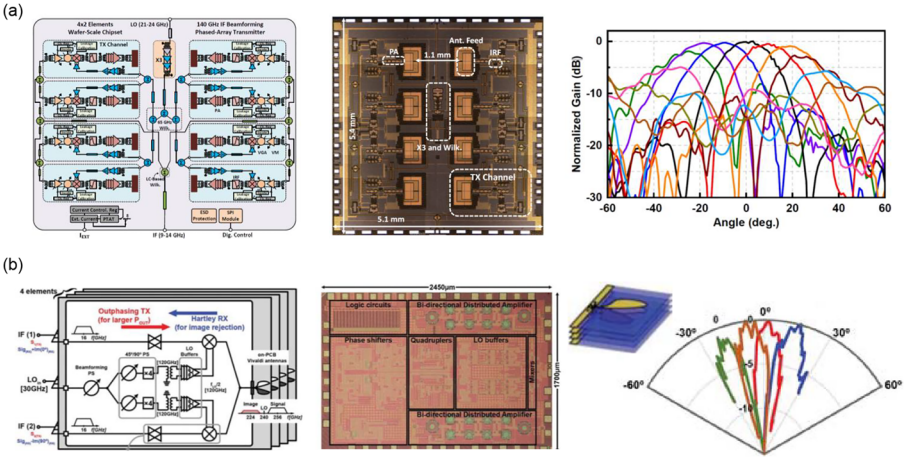

Fig. 4 **a** Eight-element 140-GHz phased array based on IF beamforming with 5-bit phase and 4-bit gain control at the IF band of 9–14 GHz [23]. Copyright 2021, IEEE. **b** 300-GHz image-rejection phased array transceiver based on a bi-directional outphasing and Hartley architecture [24]. Copyright 2021, IEEE

with a multiplicative factor at the harmonically radiated THz signal. For instance, a W-band signal with a tuning phase of 0–90° will be expanded into 0–360° when multiplied by a quadrupler to THz. Therefore, a single-ended phase shifter can suffice in many cases [28]. One significant challenge in this architecture is that the locking range can be small, and this can result in the system going out of synchronization with process variations and mismatches. To improve the network's locking range, Saeidi et al. proposed a network architecture that removes the individual oscillation ability of each element as shown in Fig. 5, and creates a condition of a collective oscillation of the 2D array as the only stable solution. This increases the locking range from 10 to 53 GHz [25, 29]. Furthermore, this architecture also enhances the locking phase angle, allowing the phase of each unit to be adjusted within a larger range for beamforming.

In addition to the works mentioned above, a comparatively large tuning beam angle of ±40° in both the E and H plane [11] has been demonstrated at 280 GHz with an array size of 4×4. A ±64°/±26° tuning has been demonstrated at 344 GHz with an array size of 2×2 [30]. A high DC-to-RF efficiency of 0.91% was reported in [31] with an array size of 1×4 and a scanning angle of ±12° in the E plane, in which a reflective-type phase shifter is used to reduce insertion loss. In [32], a phased array on a glass module has been demonstrated to improve the radiation efficiency of on-chip antennas at the D-band, with a simulated steering angle of ±20°.

Apart from the approaches to steer continuous THz waves as above, attempts to steer short THz pulses have also been considered. For example, digital-to-impulse radiating arrays have been developed based on SiGe BiCMOS, which achieves a peak EIRP of 30 dBm with a pulse width of 5.4 ps and a jitter of 270 fs by combining signals from 8 elements with a programmable delay [33]. Using bulk CMOS, a peak EIRP of 17 dBm with a pulse width of 14 ps and a jitter of 230 fs has been achieved by combining signals from 16 elements [34]. In [35–37], radiated programmable THz waveforms with dynamic waveform shaping were

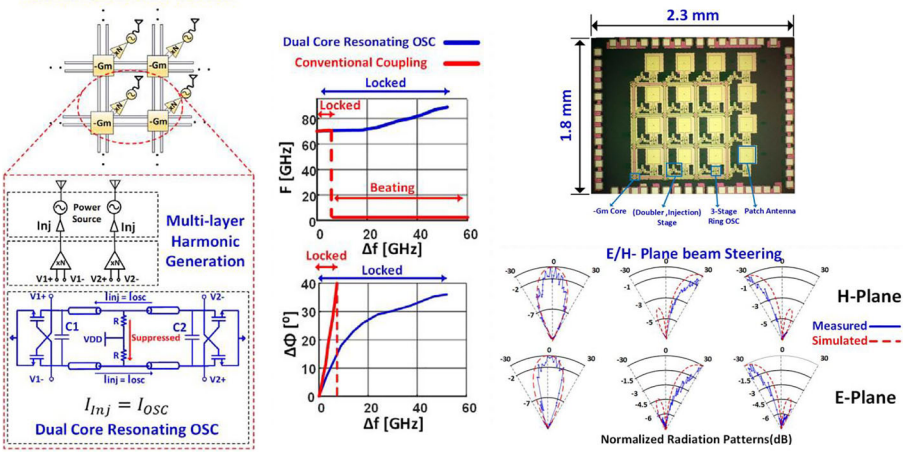

Fig. 5 416-GHz mutually coupled oscillators through transmission lines [25]. Copyright 2020, IEEE

demonstrated with the capability of generating pico-second pulses and continuous wave frequencies in a reconfigurable fashion.

2.3 THz Power Detection and Beam-Scanning Receivers

Array architectures are also important for the receiver front-ends to improve signal levels and spatial interference rejection while facilitating beam steering. Conventionally, incoherent power detection has been popular in the THz range. Examples of such detectors include Golay cells with typical noise equivalent power (NEP) in the range of 1000 pW/$\sqrt{\text{Hz}}$ [38]. Another commonly used methodology is bolometers with typical NEP in the range of 100 pW/$\sqrt{\text{Hz}}$ [39, 40]. While these methods are still often used for calibration, it is hard to miniaturize and scale them into large arrays. Integrated technologies using CMOS, SBD, III-IV, and HBT devices have been demonstrated with THz power detection abilities that satisfy many of the intended applications including the scalability for large arrays. Prior works have demonstrated CMOS/SiGe-based detectors with NEP of 10–100 pW/$\sqrt{\text{Hz}}$ [41, 42] in the 100–300 GHz range. A detector array developed with a 0.13-μm SiGe process and a CMOS-based source array operating in the 240–290-GHz range have been combined to demonstrate THz imaging capability with a sensitivity of 8.8 pW/$\sqrt{\text{Hz}}$ [43]. In [44], an electronic-photonic hybrid approach was shown for high-frequency THz imaging in the 3–3.5-THz range with a quantum cascade laser source, and a 100-pixel THz CMOS camera achieving an average NEP of 1260 pW/$\sqrt{\text{Hz}}$ between 3.25 and 3.5 THz.

With the ability to integrate antennas and detectors on the same substrate based on co-design approaches, new sensing architectures based on on-chip multiport antennas have been emerging [47–49]. As an example, a log-periodic on-chip antenna incorporating detector arrays distributed across the surface has been shown [50, 51], enabling the extraction of incident THz spectral signatures across 40–330 GHz by sensing the 2D distribution of the impressed surface current. This eliminates the requirement for on-chip wideband frequency synthesizers, mixers, and amplifiers, and miniaturizes an entire THz spectroscope to an electromagnetic scatterer and incoherent detector array compatible to subsequent linear estimation. In [45], Wu et al. modified the architecture to allow impedance control in each detector, thereby enabling the control of surface current distribution on the antenna structure. Through a nonlinear mapping between optimal digital states to incident THz field properties, a programmable THz sensor capable of accepting incident field properties across the spectrum, angle of incidence, and polarization has been demonstrated (Fig. 6(a)). The sensor demonstrated noise equivalent power of 20.4 to 274 pW/$\sqrt{\text{Hz}}$ across 0.10–1.0 THz, covering the incident angles up to $\pm 45°$. In addition to direct power detection, coherent heterodyne architectures allow the detection of phase information, which can be used further for beamforming at the receivers. Li et al. demonstrated a 140-GHz eight-element wafer-scale phased array receiver with a quartz superstrate with printed antennas. It scans up to $\pm 35°$ in the elevation angle and receives up to 9–10 Gbps data rates [52]. While most reported works focus on single beam steering, Hu et al. reported a 32-unit phase-locked heterodyne receiver array at 240 GHz (Fig. 6(b))

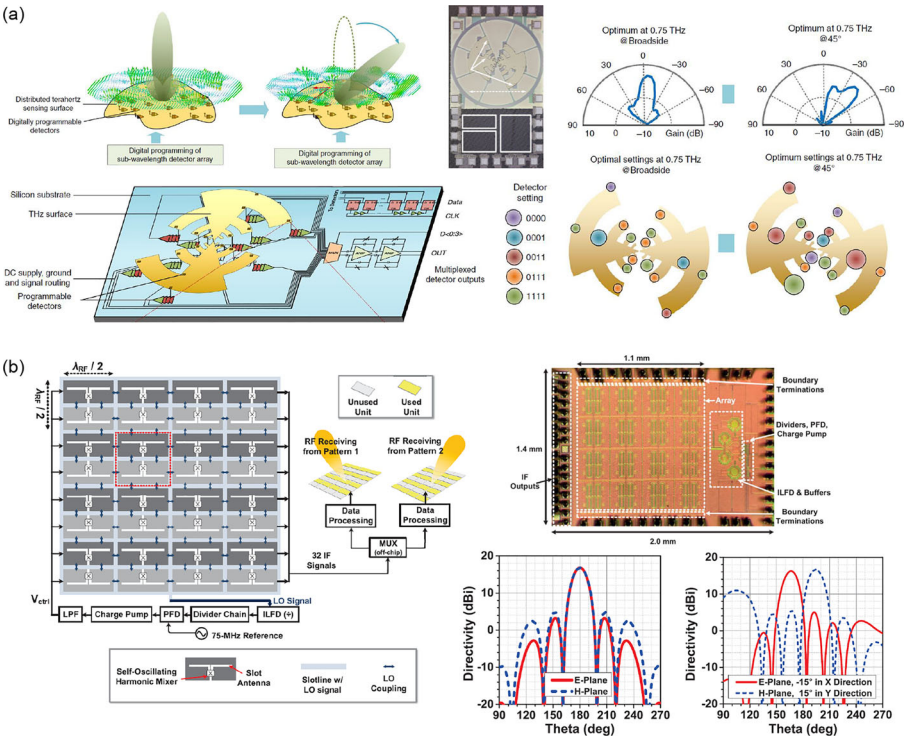

Fig. 6 **a** Distributed programmable chip-scale THz sensing interface [45]. Creative Commons Attribution (CC BY) license. **b** Heterodyne receiver array with array-wide phase locking [46]. Copyright 2019, IEEE

where the integration of two interleaved 4 × 4 arrays can allow concurrent steering of two independent beams with a sensitivity of 58 fW at a 1-kHz measurement bandwidth and a steering angle of ±20° [46]. Coherent methods show superior sensitivity versus direct detection methods by at least 40 dBm/$\sqrt{\text{Hz}}$ [53]. Nevertheless, the generation of LO signals, the absence of power amplifiers, and the deteriorated noise figure of receivers currently limit the frequency of operation of most CMOS heterodyne receivers below 500 GHz.

2.4 Optoelectronic Phased Arrays

While the recent advancement of THz electronics has allowed the implementation of electronic phased arrays as discussed ins Sections 2.2 and 2.3, the optical down-conversion approach also supports beam steering by spatially modulating photocurrent phase profiles. For example, when a photoconductive antenna is used in a reflective configuration, the THz radiation appears in the specular direction of the optical pump. Therefore, beam steering is attained by tilting the incident angle of the optical pump [57]. Instead of tilting the optical pump, an array of photconducting antennas sinusoidally biased with respect to their positions can also generate a THz pulse with a tilted wavefront [54]. By altering the bias pattern, beam steering

over 40° has been demonstrated at 480 GHz (Fig. 7(a)). The use of two pump beams with a frequency difference allows more agile beam steering. When two spatially dispersed pump beams impinge on a photoconductive antenna, a THz beam with a different frequency and phase is generated. In this case, the phase ramp formed on the photoconductive antenna varies sensitively depending on the incident angle of the pump beams. A THz beam of 600 GHz can be steered over 29° when one of the two optical pump beams is tilted over 0.155° as shown in Fig. 7(b) [55]. It is also possible to incorporate an interference pattern for the optical pumps on a photoconductive antenna, which defines a discrete phased array [58]. Meanwhile, implementing multiple photoconductive antennas, each of which can be selectively excited at different positions on a silicon lens enables beam switching. An experimental demonstration of 1D beam switching over 18° has been presented in [59] along with a numerical prospect of a 2D scanning angle of 70°. Instead of photoconductive antennas or other semiconductor substrates, the use of metasurfaces composed of nanostructured gold plasmonic metagratings with nonlinear optical properties can tailor both the phase and polarization around 1 THz in response to optical pulse excitation with a central wavelength of 1500 nm [60]. While those approaches have relied on spatial optics for optical pumping, the use of an optical fiber network that delivers an optical pump with tunable delays enables THz beam steering with an integrated platform. Che et al. have implemented an array of uni-traveling carrier photodiodes (UTC-PDs) fed with two optical laser signals via an optical fiber network [56]. By controlling the phase difference between the two laser signals based on thermo-optic effect, THz beam steering over 50° at 300 GHz has been demonstrated as shown in Fig. 7(c). The use of a true-time optical delay line enables beam steering of pulsed THz waves over 20° [61].

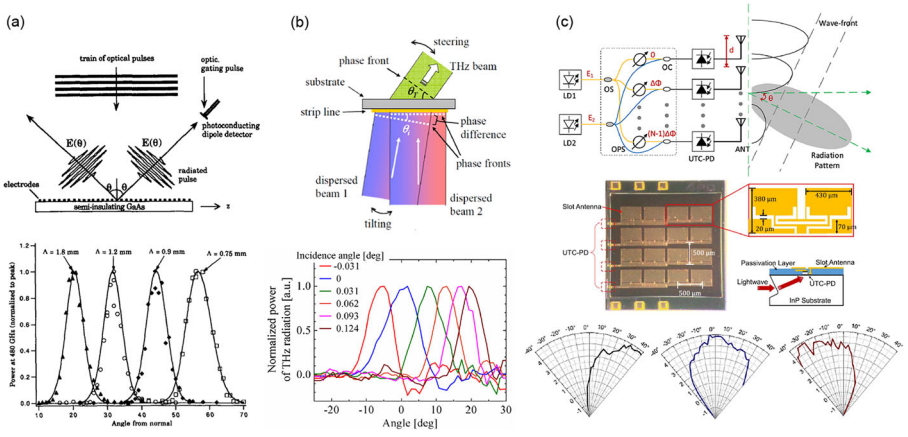

Fig. 7 **a** Photoconductive antenna array with spatially modulated voltage bias [54]. Copyright 1992, IEEE. **b** Spatially dispersed ultrafast laser pulses that generate a tilted phasefront [55]. Copyright 2008, Optical Society of America. **c** Fiber-fed optical phased array combined with arrayed photomixers [56]. Copyright 2020, IEEE

2.5 Passive Phase Shifters

Although there have been promising demonstrations of the electronic and photonic phased arrays, there is still a great technical challenge to cover an aperture size of several centimeters, which is important for practical wireless transmission of THz waves as discussed in Section 1. The realization of a passive phased array, for which only a single transmitter is required, could mitigate this challenge. A passive phased array is also advantageous in terms of its compatibility with a high-power amplifier and reversibility in transmission and reception. While the realization of a complete passive phased array has yet to be demonstrated in the THz range, there is an increasing number of efforts to implement THz phase shifters, a fundamental component of a phased array.

2.5.1 Solid-state Phase Shifters

A solid-state THz phase shifter using split-ring resonators (SRRs) fabricated on an n-doped GaAs layer shown in Fig. 8(a) was first presented by Chen et al. in [62]. It achieved a voltage-controlled linear phase shift of about 30° for the transmitted wave with the amplitude fluctuation below 10% over a bandwidth of about 23 GHz around 890 GHz. Lee et al. have developed a graphene-based metamaterial (Fig. 8(b)) to modulate the phase of the transmitted wave by 32.2° at 650 GHz [63]. Zhao et al. have used insulator-to-metal transition of vanadium dioxide (VO_2), which has a phase change temperature of 68°C, to generate a phase shift above 130° over a bandwidth of 55 GHz from 575 to 630 GHz with the maximum insertion loss of about 16 dB based on thermal excitation by laser irradiation (Fig. 8(c)) [64]. Since these approaches are based on resonance, the bandwidths are limited, and the phase shift near the resonance frequency is inseparable from amplitude variation. In addition, since they

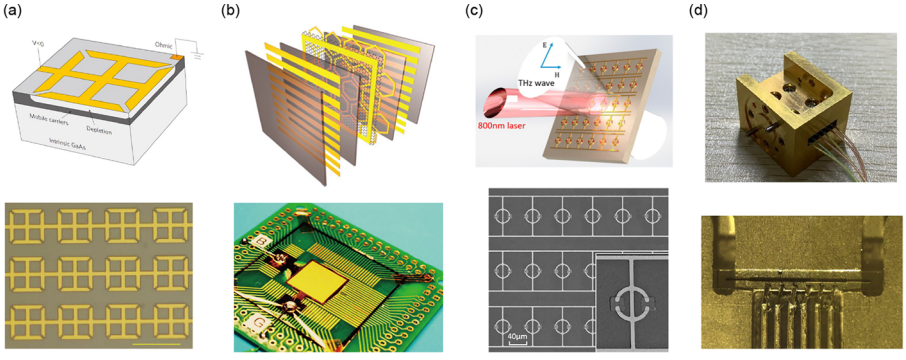

Fig. 8 **a** Split-ring resonator-based phase shifter developed on a n-doped GaAs layer. [62]. Copyright 2009, Springer Nature. **b** Gate-controlled graphene phase modulator [63]. Copyright 2012, Springer Nature. **c** Photoinduced phase control via vanadium dioxide incorporated nanostructure [64]. Copyright 2018, American Chemical Society. **d** Transmission line-coupled AlGaN/GaN layer for digital phase shift [65]. Copyright 2021, Springer Nature

are used in transmissive configuration, the refractive index mismatch between the semiconductor substrate and free-space involves reflection losses.

There are other approaches based on non-resonant structures suited for broadband operation. The use of a checkerboard metal pattern in which metal patches are interconnected via VO_2 can switch its response from capacitive to inductive by thermal phase transition, resulting in a phase shift of 90° at 470 GHz with 8 dB insertion loss [66]. An array of gated two-dimensional electron gas formed by a layer of AlGaN/GaN coupled to a transmission line (Fig. 8(d)) enables phase manipulation with a precision of 2 to 5° at frequencies from 0.26 to 0.27 THz, with an average phase error of 0.36° [65]. A concept of variable delay lines using gated graphene transmission lines has also been considered numerically [67]. As compared to the resonant structures, the non-resonant structures allow broader bandwidths at a cost of weaker perturbation to the wave propagation.

2.5.2 Liquid Crystal Phase Shifters

Liquid crystals possess an electrically controllable refractive index based on birefringence, which has been considered for THz frequencies [71–73]. To implement THz phase shifters using liquid crystals, reconciling transparency with tunability is important. While the early works have used simple electrodes so that THz waves do not impinge on the electrodes [74, 75], more recent works have improved the structures and the materials of the electrodes. Those include the use of metal grating [76, 77], graphene [78, 79], ITO nanowhiskers [68, 80], and PEDOT: PSS [81, 82]. The use of a graphene thin layer as electrodes allows not only transparency but also direct current voltage application without ion diffusion problems [78]. The ITO nanowhiskers can serve both as a transparent electrode and an alignment layer [68] as shown in Fig. 9(a). The performance of the phase shifters can be characterized by a figure of merit, which is the amount of a phase shift normalized by the insertion loss and bias voltage. It takes a value of around 4.6–7.7° $dB^{-1} \cdot V^{-1}$ for the recent liquid crystal

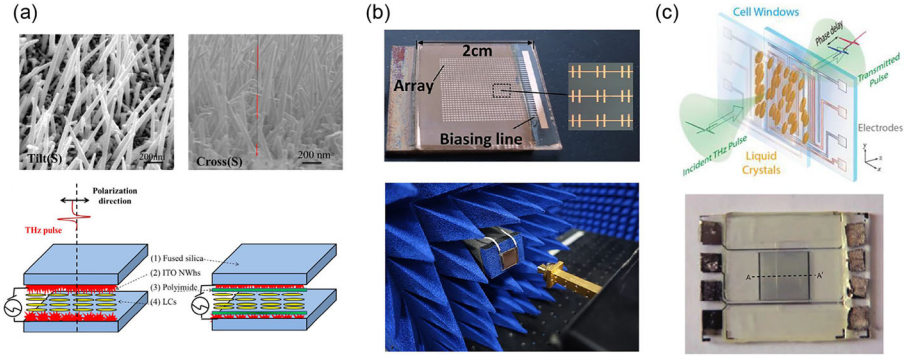

Fig. 9 **a** Indium-tin-oxide nanowhiskers for biasing liquid crystal THz phase shifters [68]. Copyright 2014, AIP Publishing. **b** Reflective liquid crystal THz phase shifter [69]. Copyright 2014, AIP Publishing. **c** Fast switching design based on an active alignment of liquid crystals both in- and out-plane orientations [70] Copyright 2018, IEEE

phase shifters [83]. Thus, the implementation of 360° phase shift still requires high voltage and insertion loss. The introduction of subwavelength artificial structures is expected to enhance the phase shift. For example, an array of resonant metal patches serving both as a reflector and a liquid crystal electrode (Fig. 9(b)) has shown a phase shift over 350° for frequencies from 353.5 to 359.3 GHz at 40 V with a loss above 12 dB [69]. A subwavelength array of dielectric resonators can be designed to enhance rotation force on liquid crystal molecules via the surface anchorage force [84], enabling a 1.8 times higher phase shift at 700 GHz than without the structure. The use of resonant structures, however, poses a limitation on the bandwidth. Another research direction is to improve the switching speed. Ung et al. have developed an electrode structure that actively switches liquid crystal molecules in both the in-plane and out-plane directions (Fig. 9(c)), enabling high-speed operation of about 0.5 s [70].

In addition to implementing phase shifters, direct beam switching using liquid crystals is also possible. Scherger et al. have demonstrated that the angle of emergence from a wedge-shaped liquid crystal container can be deflected by 6.3° for frequencies from 300 to 600 GHz by bias voltage [85].

2.5.3 Electromechanical Phase Shifters

As reviewed in Sections 2.5.1 and 2.5.2, the solid-state and liquid crystal phase shifters are still facing fundamental challenges in terms of insertion losses. To circumvent the severe losses, the use of micromechanical devices has recently been considered for THz phase shifters. For example, Shah et al. have developed an array of electrostatically switchable E-plane stubs incorporated on a waveguide wall as shown in Fig. 10(a) functioning as a phase shifter at around 500 GHz [86]. By selecting the blocking/unblocking states of each stub, a 10-step phase shift up to 20° with a 3 dB insertion loss, of which 0.5-1.5-dB is attributed to the MEMS structure, at

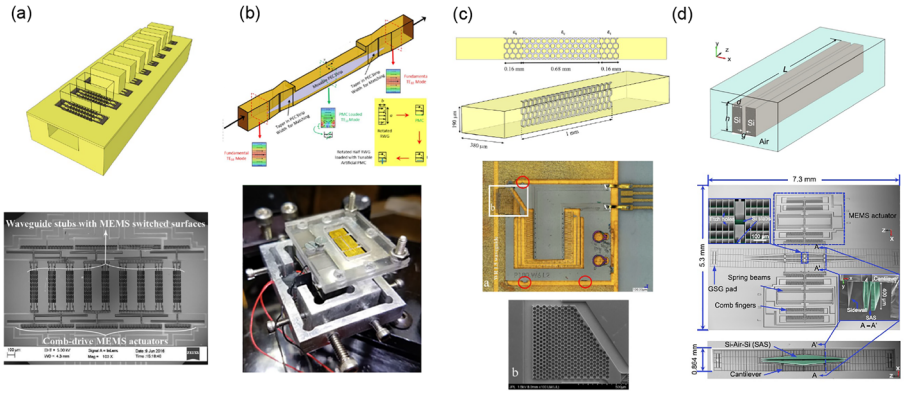

Fig. 10 **a** Electrostatically switchable E-plane stub array on a waveguide [86]. Copyright 2016, IEEE. **b** Piezoelectric-based movable metal strip in a waveguide [87]. Copyright 2018, IEEE. **c** Electrostatically movable perforated silicon slab inserted in a waveguide [88]. Copyright 2018, IEEE. **d** Silicon-air-silicon structure with a mechanically tunable gap [89]. Copyright 2021, IEEE

500–550 GHz has been demonstrated. Ibrahim et al. have presented a piezo-based movable metal strip that modulates the dispersion relation in a waveguide as shown in Fig. 10(b) [87]. It generates a phase shift of 380° with a maximum insertion loss of 3 dB at 230–250 GHz. The phase shift can be continuously tuned by the vertical displacement of the strip. Rahiminejad et al. have developed a perforated silicon slab inserted into a waveguide to modulate the effective mode refractive index by displacing the slab as shown in Fig. 10(c) [88]. The maximum phase shift of 145° with an insertion loss of 1.8 dB, for which 1.6 dB is intrinsic to the waveguide, has been demonstrated at 550 GHz. Zhao et al. have used a supermode supported on a silicon-air-silicon structure inside a waveguide with a micromechanically tunable gap as shown in Fig. 10(d) [89]. The maximum phase shift of 550° with an insertion loss of 1.87 dB has been achieved at 330 GHz. The figure of merit of 375°/dB is currently the highest among any of the THz phase shifters.

The micromechanical phase shifters are thus promising for low-loss THz phase shifters although they work only at a limited speed. Moreover, extending it into an array poses another challenge considering that the movable parts inside the waveguides are supported by larger mechanical components external to the waveguide.

3 Reconfigurable Diffraction on Variable Structures

As reviewed in Section 2, the implementation of large-scale THz phased arrays still requires considerable research efforts. Meanwhile, alternative approaches to passively control diffraction have also been considered. There are two major approaches: a variable diffractive structure enabling beam steering for a fixed frequency and a fixed diffractive structure enabling beam steering by sweeping the frequency. We review the former in this section and the latter in Section 4. The variable structures are designed to generate a reconfigurable spatial phase distribution. Being decoupled from power generation, the use of passive structures for beam steering allows heterogeneous integration of high-efficiency and high-power THz sources, even including gyrotrons [90].

3.1 Lenses

While a lens is a fundamental component for beamforming, it can also be used for beam steering by tweaking the configuration. For example, Alonso et al. demonstrated THz beam steering by spatially varying the excitation point of a hemispherical silicon lens using a piezoelectric actuator [91]. Using a setup shown in Fig. 11(a), a beam with a 3-dB beamwidth of 8° can be continuously tilted nearly to ±25° with a scan loss of 0.6 dB at 550 GHz. The concept has been extended to a larger array shown in Fig. 11(b) based on a leaky-wave feeding structure coupled with a lens array [92]. By combining phase shift on a sparse array with a mechanical translation of the lens array, beam steering over ±25° with an antenna gain above 35 dB can be expected.

Another approach is to use a Luneburg lens, which is a distributed index lens with a radially decreasing refractive index from $\sqrt{2}$ to 1. It allows a conversion of point

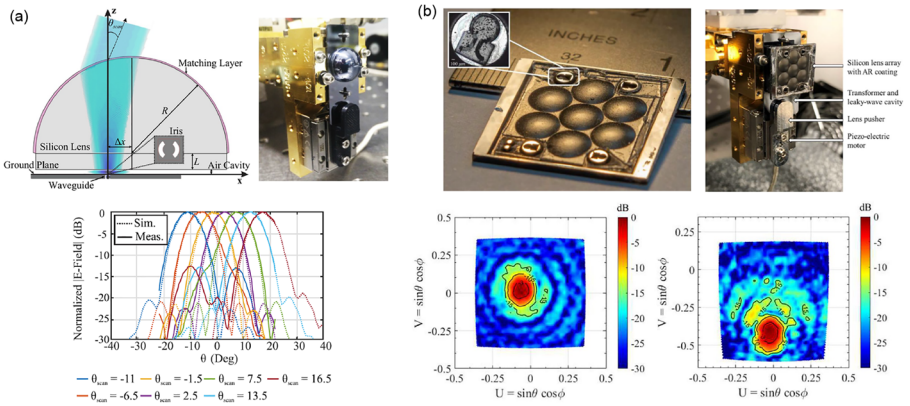

Fig. 11 **a** A hemispherical silicon lens with a movable excitation point using a piezoelectric actuator [91]. Copyright 2018, IEEE. **b** Scanning lens-phased array with multimode leaky-wave feeding [92]. Creative Commons Attribution (CC BY) license

excitation on its circumference into a collimated beam in free-space [96]. Since each point on the circumference is mapped to the respective beam direction, beam steering is enabled by altering the excitation point. Headland et al. have implemented a low-loss THz Luneburg lens using an effective medium defined by a perforated silicon substrate as shown in Fig. 12(a) [93]. To feed the lens, an array of seven photonic crystal waveguides is incorporated on the same substrate as input ports connectable to a hollow metal waveguide. By switching the excitation ports, discrete beam steering with a total coverage of 120° from 320 to 390 GHz has been demonstrated. It is also possible to generate multiple beams by exciting several ports simultaneously. For efficient power extraction from the lens, the refractive index at the circumference should be close to 1, which is challenging with an effective medium approach. Amarasinghe et al. have presented a possible solution to this challenge by using dielectric-filled conducting plates with curved surfaces, which has been designed for around 162 GHz [97]. Since the effective refractive index of the fundamental TE mode in air-filled conducting plates varies from 0 to 1 depending on the plate separation, insertion of a dielectric material with a refractive index of n extends this range from 0 to n. Such a design can be further extended based on transformation optics [94] so that beam steering over 50° from 130 to 180 GHz is attained by displacing the excitation point along the straight edge as shown in Fig. 12(b). Instead of moving the excitation point, a variable Luneburg lens that can couple to a fixed port has also been presented [95]. A pair of metal plates with a curved surface separated by air has been designed for around 300 GHz (Fig. 12(c)). When tilting the plate from $-25'$ to $+25'$ ($-0.42°$ to $+0.42°$), the beam can be steered from -25 to $+25°$ as a result of trajectory deflection inside the lens. Thus, a small mechanical tilt can be amplified to a large beam deflection, which is 60 times in the presented work.

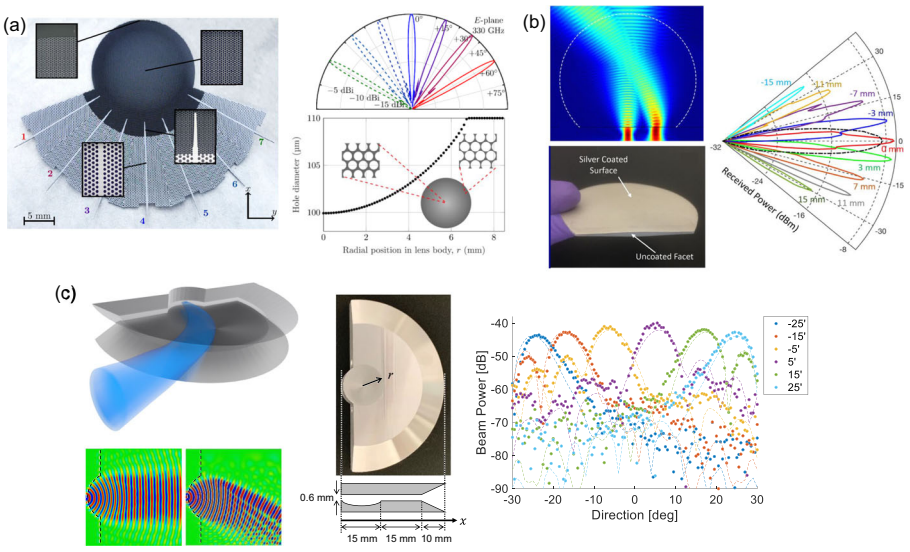

Fig. 12 **a** Effective medium Luneburg lens made of a high-resistivity silicon substrate fed via photonic crystal waveguides [93]. Creative Commons Attribution (CC BY) license. **b** Silver-coated Teflon substrate optimized for broadband and wide-angle beam steering [94]. Creative Commons Attribution (CC BY) license. **c** Dielectric-Free Luneburg lens with internal trajectory deflection controlled by relative tilt [95]. Copyright 2020, IEEE

3.2 Grating

Diffraction gratings composed of periodic structures have been commonly used to alter beam directions in transmissive and reflective configurations as conceptually illustrated in Fig. 1(c) and (d), respectively. When a periodic structure is illuminated by a uniform wavefront, the diffracted wavefront acquires a tilted phasefront depending on the periodicity and the frequency. Therefore, the beam can be steered if the grating periodicity is variable. It should be noted that the bandwidth thus transmitted in a certain direction is limited since the beam direction is frequency-dependent. However, this feature can also be used for beam steering by sweeping the frequency as explained in Section 4.

Chan et al. have demonstrated a solid-state THz spatial light modulator composed of a 4×4 matrix of reconfigurable metamaterial absorbers fabricated on an n-doped GaAs layer (Fig. 13(a)) [98]. By controlling the bias voltage, a virtual double-slit has been created, which can generate variable diffraction patterns at 360 GHz when switching the spacing from 8 to 12 mm. Lin et al. have presented a liquid crystal transmissive phase grating composed of an array of liquid crystal cells spaced by metal plates [103]. By modulating the phase contrast with bias voltages, the ratio of the 0th- to 1st-order diffractions can be tuned from 10 to 1 at 300 GHz. There are more reports on implementing variable transmissive gratings using photo-induced carriers, which can be created in a semiconductor substrate by an optical pump above the band gap energy. For example, a high-resistivity silicon wafer with a thickness

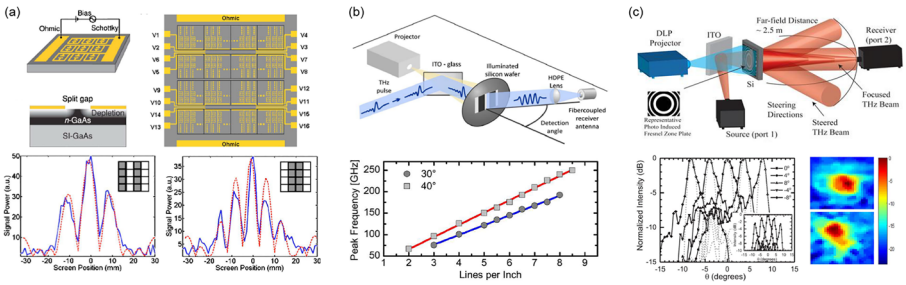

Fig. 13 **a** THz spatial light modulator based on 4 × 4 metamaterial absorbers [98]. Copyright 2009, AIP Publishing. **b** Linear grating defined by photo-induced carriers on a high-resistivity silicon substrate [99]. Copyright 2012, Optical Society of America. **c** Fresnel zone plate defined by photo-induced carriers on a high-resistivity silicon substrate [100]. Copyright 2017, IEEE

of 500 μm illuminated with a mercury arc lamp of 2 W/cm^2 (Fig. 13(b)) can steer a beam from 30 to 40° for frequencies around 200 GHz by varying the illumination pitch [99]. Instead of a simple 1D grating, a Fresnel zone plate can also be implemented on a high-resistivity silicon wafer (Fig. 13(c)), with which 2D beam steering is enabled at 740 GHz [100]. The implementation of a blazed refractive index grating on a GaAs layer pumped by a spatially modulated optical pump has also been demonstrated to allow asymmetric THz diffraction between ±30° [104]. Although the use of photo-induced carriers thus offers arbitrarily shaped amplitude gratings, it involves conductive loss during transmission and also reflection loss between the wafer and air.

In the optical regime, micro-electromechanical-systems (MEMS) consisting of an array of vertically movable cantilevers are widely used as reconfigurable reflective gratings [105]. However, their micro stroke is too small to generate sufficient phase contrast for the THz wavelengths. To implement a meso-scale stroke of an order of

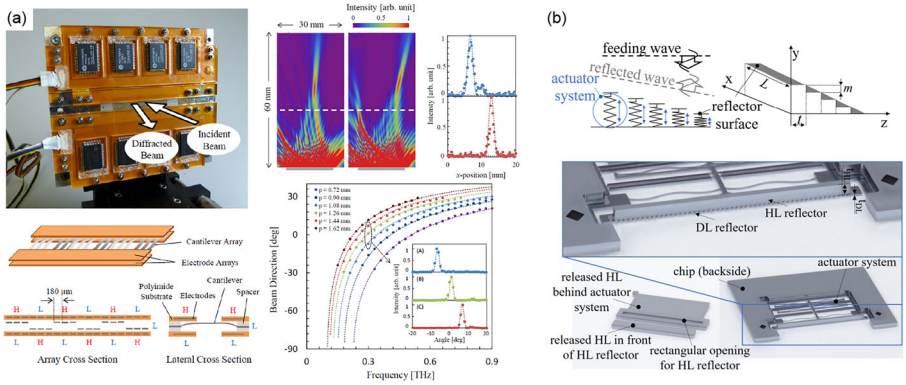

Fig. 14 **a** Electrostatically actuated cantilever array serving as a programmable grating [101]. Copyright 2013, Optical Society of America. **b** High-resolution height control of electrostatic actuators enabling a blazed grating [102]. Copyright 2021, IEEE

0.1 mm, a grating consisting of a subwavelength cantilever array aligned in a 180-μm pitch defined by etching a metal film has been presented [101] (Fig. 14(a)). By changing the periodicity based on the electrostatic actuation of each cantilever with a vertical stroke of 80 μm, the 1st-order diffraction beam can be steered over 40° at 300 GHz. Another approach of continuous periodicity tuning has been presented using a loudspeaker as an actuator that laterally compresses a 3D-printed grating to vary the grating period from 3.09 to 3.20 mm, thereby tilting the beam over 2.6°, at a speed of 60 Hz [106]. Meanwhile, those gratings with a binary surface are accompanied by the undesirable 0th-order diffraction, i.e., the specular reflection. The 0th-order diffraction can be effectively removed using a blazed grating. Schmitt et al. have proposed a reconfigurable blazed grating implemented by electrostatically tuning the local heights of a segmented surface [107]. The diffraction property of such a surface has been numerically investigated in detail [108]. Based on this concept, an electrostatic actuator incorporating a mechanical amplifier, which can linearly resolve a total displacement of 150 μm in 8 steps, has been developed [109] with a potential to implement a tunable blazed grating above 300 GHz[102] as shown in Fig. 14(b). Experimental demonstration using static grating samples with an optimized surface profile shows promising results at 300 GHz [110]. Another attempt of developing a metagrating at 140 GHz, which suppresses undesired diffraction orders, has been demonstrated to cover a conical 3D space by mechanical compression and rotation of the grating [111].

3.3 Metasurfaces

Metasurfaces are 2D metamaterials engineered to have artificial electromagnetic properties based on subwavelength periodic structures. The amplitude and phase change typically relies on an abrupt change of the surface current distribution on the boundaries of unit cells, suggesting a potential for dynamic control with various mechanisms including CMOS/HEMT devices, graphene, liquid crystal, and MEMS. In the microwave range, such modulation has been implemented using electronic components [112–115]. In the THz range, an early demonstration has been performed by Chen et al. [116], in which a split-ring resonator is manufactured on a GaAs substrate so that SBDs are formed on the substrate.

However, diode-based tuning methods effective at microwave frequencies may suffer from an increasing loss at the THz range. The use of CMOS can be an effective alternative to realize scalable THz metasurfaces. Venkatesh et al. presented a programmable THz metasurface composed of tiled CMOS ring elements with individual reconfigurability as shown in Fig. 15 [117, 118]. To allow reconfigurability beyond the cut-off frequency of the devices, a novel active meta-element structure was developed, in which the device parasitic capacitance resonates with multiple inductive loops within the subwavelength structure. It functions as a high-speed programmable THz metasurface at 0.3 THz, which implements nearly arbitrary spatial amplitude (up to 25 dB) and phase control (up to 260°) enabling rapid beam steering covering ±30° and holographic projections reconfigurable up to 5-GHz clock frequencies. Metasurfaces based on CMOS SRRs have also been developed to shift resonance frequencies

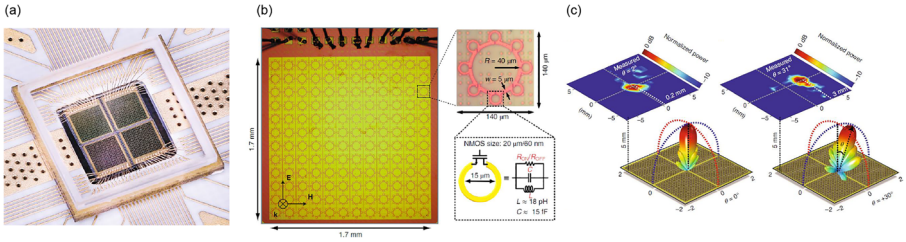

Fig. 15 High-speed CMOS programmable metasurface for beamforming and hologram [117]. **a** Chip photo. **b** Inductor ring design. **c** Farfield beamforming at 0° and 30°. Copyright 2020, Springer Nature

over 35 GHz at 0.3 THz [119]. HEMT devices generally allow higher operating frequencies. Zhang et al. have presented HEMT-based SRRs in which dipole resonance and inductor-capacitor resonance are combined to achieve a modulation depth of 85% at 0.35 THz [120].

At the higher frequencies where both CMOS and HEMT devices are hard to operate, graphene and liquid crystal–based methods can be used [121]. Graphene is a two-dimensional carbon material with electrically tunable conductivity. Unlike CMOS-based methods that rely on narrow-band resonance, graphene-based structures can support high bandwidths even beyond 1 THz with considerable modulation depth and large array scalability. Also, 360° phase shift between 1.1 and 1.5 THz has been demonstrated with a loss ranging from 0.5 to 6 dB [122]. An early demonstration of a graphene-based reconfigurable aperture composed of a 4×4 array [123] has recently evolved into a 16×16 array (Fig. 16(a)) [124]. The flexibility of graphene metasurfaces is advantageous for fine wavefront tuning for multi-beam steering, which will be important for signal transmission into multiple directions, and has recently been studied in numerical analyses [125–128]. Liquid crystal can be another candidate for THz manipulation although it typically requires high voltages and a long response time. In [129], liquid crystal metamaterial spatial light modulator (Fig. 16(b)) has attained 75% modulation depth at 3.67 THz. A liquid crystal–based reflective metasurface operating at 672 GHz has been demonstrated with a steerable

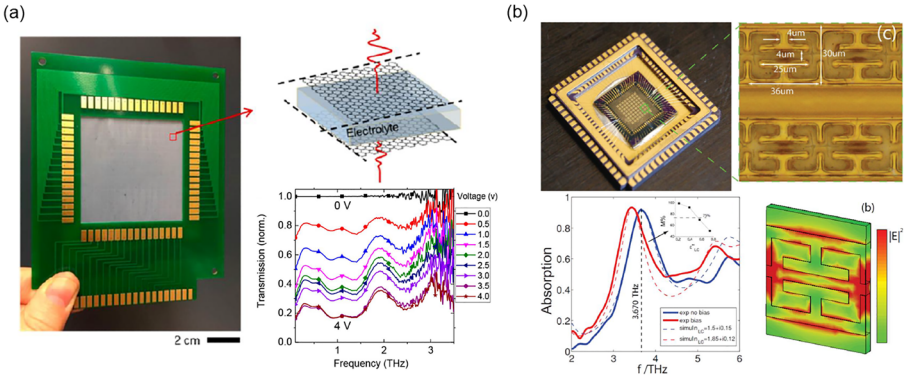

Fig. 16 **a** Graphene-based THz spatial light modulator [124]. Copyright 2020, American Chemical Society. **b** Liquid crystal-filled THz spatial light modulator [129]. Copyright 2014, John Wiley and Sons

range of 32° [130]. In [131], a 408-GHz liquid crystal-based transmissive metasurface based on Fano resonance has been shown with a steerable range of 30°. Other tunable materials including VO_2 and chalcogenide are also candidates for THz signal modulation. Those materials not only respond to voltage application but also thermal excitation, bringing more degree of flexibility and potential for system integration. By exploiting the phase change property of VO_2, a phase shift over 90° at 70 GHz bandwidth and a modulation depth of 71% at 0.79 THz can be expected [132]. Hashemi et al. demonstrated a VO_2-based metasurface operating at 100 GHz offering up to 44° beam deflection in both E/H planes [133]. Besides the adoption of exotic materials, Cong et al. have demonstrated modulation based on photo-induced carriers in silicon generated by ultrafast femtosecond laser pulses [134].

As reviewed in Section 3.2, the quasi-optical property of THz waves suggests that MEMS can be used to control diffraction by directly changing the physical geometry of metasurfaces (Fig. 17). Kappa et al. have demonstrated a micromirror array operating as a spatial modulator at 0.97 to 2.28 THz, in which 768 micromirror elements with a length of 220 μm and a width of 100 μm composing a 4×6 meta pixels enable a modulation depth of 3 dB [135]. Manjappa et al. have formed Fano resonator elements with MEMS. Independent control of the two arms in the elements can define four distinct states, exhibiting XOR and XNOR operations applicable to secure wireless communication at 0.77 THz [136]. The use of MEMS allows low insertion losses and high bandwidths, at a cost of slower response rates and shorter lifetimes as compared to the semiconductor solutions.

4 Frequency Sweep on Dispersive Structures

4.1 Parallel Feeding: Gratings and Metasurfaces

The diffraction gratings and metasurfaces reviewed in Section 3 also enable beam steering based on frequency sweep because different frequency components are dispersed in different directions. In this case, the structures can be static, and the

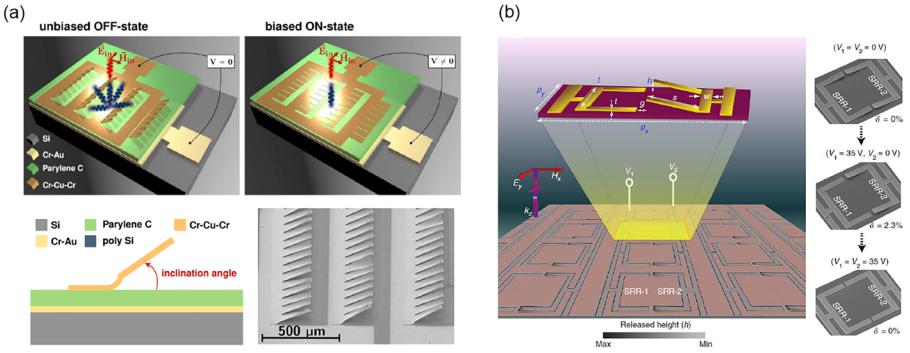

Fig. 17 **a** Wideband MEMS-based metasurface [135]. Creative Commons Attribution (CC BY) license. **b** MEMS-based tunable Fano resonator surface [136]. Creative Commons Attribution (CC BY) license

implementation is significantly simplified [137–140]. For example, such metasurfaces can unnecessitate control signal lines and be fully planar as shown in Fig. 18(a). The diffractive components are usually fed with a plane-wave using spatial optics, which implements parallel feeding that excites each point of the aperture coherently. While the diffractive components thus require additional free-space in front of the structure, it is also possible to design low-profile diffractive components compatible to point source excitation. For example, Yi et al. have demonstrated an array of 3D-printed dielectric posts with spatially varying heights as shown in Fig. 18(b) which steers a beam over 14° when swept from 225 to 325 GHz [141]. Camblor et al. have proposed a feeding network with linearly varying lengths that can generate a frequency-dependent phase gradient [142]. By cascading such layers so that a 2D aperture is formed and excited, 2D beam steering covering 50° × 45° can be attained when swept from 220 GHz and 320 GHz (Fig. 18(c)).

4.2 Serial Feeding: Leaky-Wave Antennas

In addition to the parallel feeding systems reviewed in Section 4.1, serial feeding systems can also be developed in the form of leaky-wave antennas [1]. A leaky-wave antenna generates a directional beam by successively leaking a traveling wave in a waveguide into free-space. The wavefront of the leaky-wave is thus defined by the spatial phase profile along the waveguide, which evolves linearly as the wave travels. Since the phase profile acquires a frequency-dependent linear ramp, the direction of the leaky-wave can be tilted by sweeping the frequency. A leaky-wave antenna can be regarded as a special case of a grating or a metasurface for which an incident wave is given as a guided wave as illustrated in Fig. 1(e). Thus, a serial feeding network and a radiation aperture can be merged in one package. While leaky-wave antennas have been used for decades in the microwave range [1] and also in the optical regime known as grating couplers [145], they have gained increasing attention in the THz range recently because of their beam steering capability without relying on phase shifters.

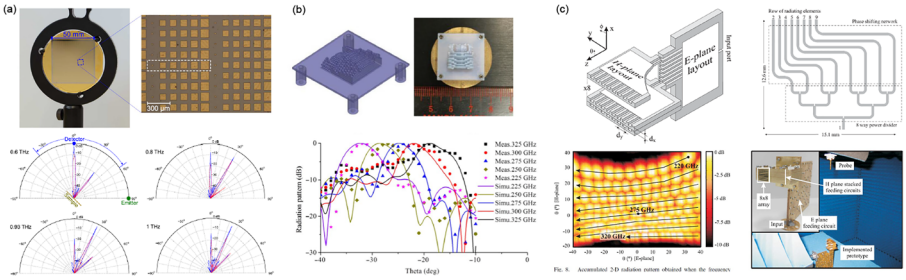

Fig. 18 **a** Resonant microstrip patches on a dielectric substrate serving as a static reflectarray [137]. Copyright 2013, Optical Society of America. **b** 3D-printed dielectric post array with spatially varying heights that allows transmissive frequency scanning [141]. Copyright 2013, IEEE. **c** 2D frequency scanning enabled by a network of feeding lines with different lengths [142]. Copyright 2013, IEEE

4.2.1 Slow-Wave Type

The leaky-wave antennas are classified into slow-wave and fast-wave types depending on the phase velocity in the waveguide. The slow-wave type is constructed with a waveguide in which the phase velocity is slower than in free-space. This usually applies to a waveguide with a dielectric substrate. Since a slow-wave is non-radiative and confined in the waveguide, periodic scatterers are required to launch a leaky-wave into free-space.

Murano et al. have developed a low-loss microstrip periodic leaky-wave antenna around 300 GHz by patterning copper on a polymer film of COP (cyclo olefin polymer) as shown in Fig. 19(a) [143]. Periodic stubs incorporated on the microstrip line convert a guided wave in the Q-TEM mode into a TE-polarized directional beam. A directional beam with a width of 4° can be steered over 38° from −23 to 15° across the broadside by sweeping the frequency from 235 to 325 GHz. The bandwidth transmitted to a certain beam direction is about 10 GHz. Fabrication of a similar periodic leaky-wave antenna on a low-loss InP substrate (Fig. 19(b)) has also been demonstrated by Lu et al. [144]. It allows monolithic integration of semiconductor sources and detectors. By sweeping the operating frequency from 230 to 330 GHz, the beam can be steered over 88° from −46 to 42° with an average beamwidth of 10°. Also, the InP substrate has a high relative permittivity of 12.4, which allows dense grating implementation advantageous for grating lobe suppression. A similar design has also been developed to steer a beam over 33° from 6 to 39° within 280–330 GHz [146]. There, the beamwidth and bandwidth attained with an external hemicylindrical

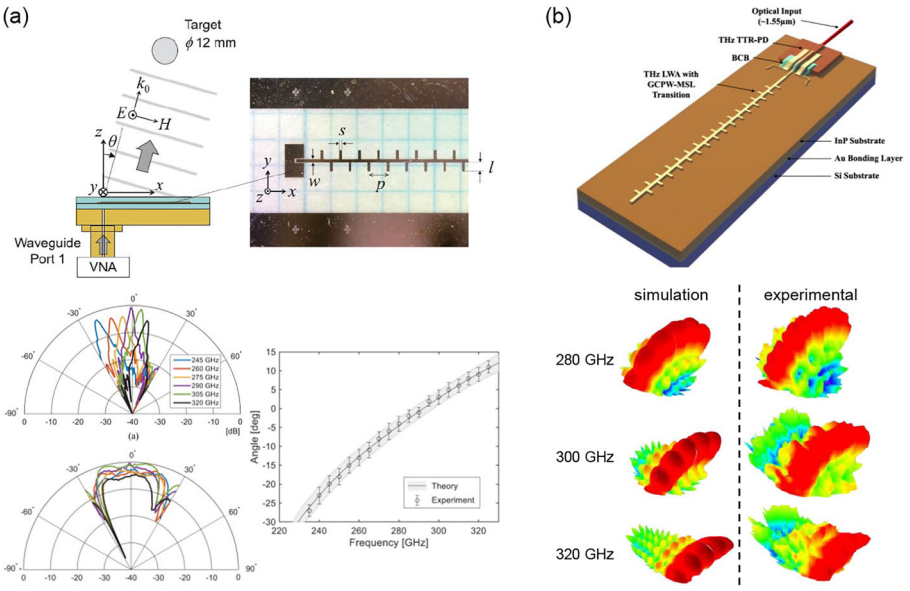

Fig. 19 **a** 300-GHz microstrip periodic leaky-wave antenna made of copper patterned on a polymer film [143]. Copyright 2017, IEEE. **b** 300-GHz microstrip leaky-wave antenna on an InP substrate [144]. Creative Commons Attribution (CC BY) license

Teflon lens are 9° and 12 GHz, respectively. As discussed in Section 1, practical THz beam steering will require a centimeter-scale antenna aperture. While the use of a semiconductor substrate allows low-loss and monolithic integration with other components, the use of a polymer substrate enables the implementation of a large aperture at a low cost. Such a trade-off should be considered when designing a leaky-wave antenna.

Apart from the frequency scanning approach, fixed frequency beam steering with a leaky-wave antenna has also been considered using reconfigurable impedance surfaces. Launching surface waves supported on an electrically reconfigurable impedance surface has been numerically considered based on MEMS [147] and graphene [148–154]. By varying the grating pattern, beam steering will be attained without frequency sweep. Still, the use of a grating involves frequency dispersion and limits the bandwidth in each direction.

4.2.2 Fast-Wave Type

Leaky-wave antennas of the fast-wave type are usually constructed with a hollow metallic waveguide or a left-handed metamaterial waveguide, in which the apparent wavelength becomes longer than in free-space. In this case, the traveling wave spontaneously leaks into free-space when the fields inside and outside the waveguide have a continuous boundary, for example when a slot is created on the metallic waveguide wall. This is in contrast to the slow-wave type, for which a grating is indispensable to launch the non-radiative traveling wave into free-space.

As compared to the microwave range, requirements for fabrication tolerance and surface roughness of a metallic waveguide become severer in the THz range. One approach to tackle this challenge is to adopt silicon micromachining [157]. Precisely processed silicon substrates metalized with gold can define low-loss THz metallic waveguides. Based on this concept, Gomez-Torrent et al. have developed a low-profile and high-gain leaky-wave antenna, in which an integrated parabolic reflector generates a planar wavefront that uniformly feeds the two-dimensional aperture as shown in Fig. 20(a) [155]. By sweeping from 220 to 300 GHz, the beam is steerable from 15 to 65° with an average radiation efficiency of −1 dB and a maximum gain of 28.5 dBi. Wu et al. have attained low sidelobe and cross-polarization levels by developing a parallel array of four tapered radiation slots designed to cancel cross-polarization components [158]. The measured sidelobe and cross-polarization levels are about −25 dB and −30 dB, respectively, while the peak gain and radiation efficiency are 21.3 dBi and 34.7% at 395 GHz, respectively. By sweeping the frequency from 390 to 410 GHz, the beam direction can be varied from 45 to 48° with a 3-dB beamwidth of about 5°. Although the phase matching condition of the fast-wave type usually allows only forward beam steering, Sarabandi et al. have developed a method of forward and backward beam steering across the broadside by employing a meander propagation path to insert extra phase shift between adjacent radiation elements [159]. The array generates a beamwidth of about 2.5° with a steerable from −25 to 25° by sweeping the frequency from 230 to 245 GHz. The antenna directivity above 29 dBi and a radiation efficiency of more than 55% have been demonstrated.

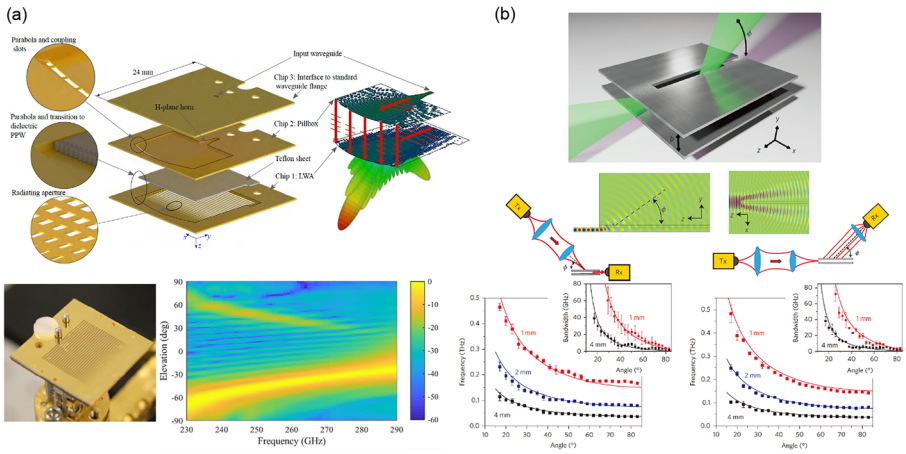

Fig. 20 **a** 300-GHz high-gain leaky-wave antenna with an integrated parabolic reflector for uniform aperture feeding [155]. Creative Commons Attribution (CC BY) license. **b** THz leaky-wave antenna implemented with a slot on a parallel plate metal waveguide in the TE1 mode [156]. Copyright 2015, Springer Nature

The hollow metallic waveguides involve major conductive losses due to the H-plane walls perpendicular to the electric field. Accordingly, the removal of the H-plane walls can suppress the transmission losses. This situation is equivalent to use a parallel plate metallic waveguide in the TE1 mode, which has been presented as a simple alternative to implement a THz leaky-wave antenna by Karl et al. as shown in Fig. 20(b) [156]. The leaky-wave can be launched from a slot incorporated on the top plate, and the beam direction changes from 5 to 80° when the frequency varies from 150 to 500 GHz. The slot width profile along the propagation axis is an important design parameter for beam pattern optimization [160].

It has been known that composite right/left-handed transmission lines can also sustain fast-waves [161]. Tavallaee et al. have developed such a leaky-wave antenna monolithically integrated with a quantum cascade laser [162]. Discrete beam steering over 25° has been demonstrated when the frequency is swept from 2.65 to 2.81 THz at 77 K. The authors discussed that it will be possible to cover backward beam steering by inserting series capacitance to implement negative phase velocity.

4.2.3 2D Leaky-Wave Antennas

The leaky-wave antennas reviewed in Sections 4.2.1 and 4.2.2 are with 1D apertures that generate a fan beam collimated in one plane but uncollimated in the orthogonal plane. A parallel array of such 1D leaky-wave antennas can define a 2D aperture that generates a pencil beam collimated in both of the two orthogonal directions, and 2D beam steering is attained when each line is fed with variable phases. Camblor et al. have developed parallel feeding lines with linearly varying lengths that generate

a variable phase ramp based on frequency sweep [163]. The hybrid combination of serial and parallel arrays enables 2D beam steering composed of slow tilt in the column direction and fast tilt in the row direction, covering a domain of 20° × 60° by frequency sweep from 240 to 310 GHz as shown in Fig. 21(a). Redundancy of the footprint of the feeding lines can be further compressed towards a compact system as shown in Fig. 21(b) [164]. While these approaches are promising for fully electronic 2D beam steering with a simple structure, it should be noted that the bandwidth transmitted in each direction becomes narrower than the 1D leaky-wave antennas.

Sato et al. have proposed another approach to implement 2D beam steering based on trajectory deflection of a leaky mode as shown in Fig. 21(c) [165]. Using a pair of metal plates with a mesh surface, in which the trajectory of the leaky mode is controllable, the beam direction can be steered vertically by frequency sweep and

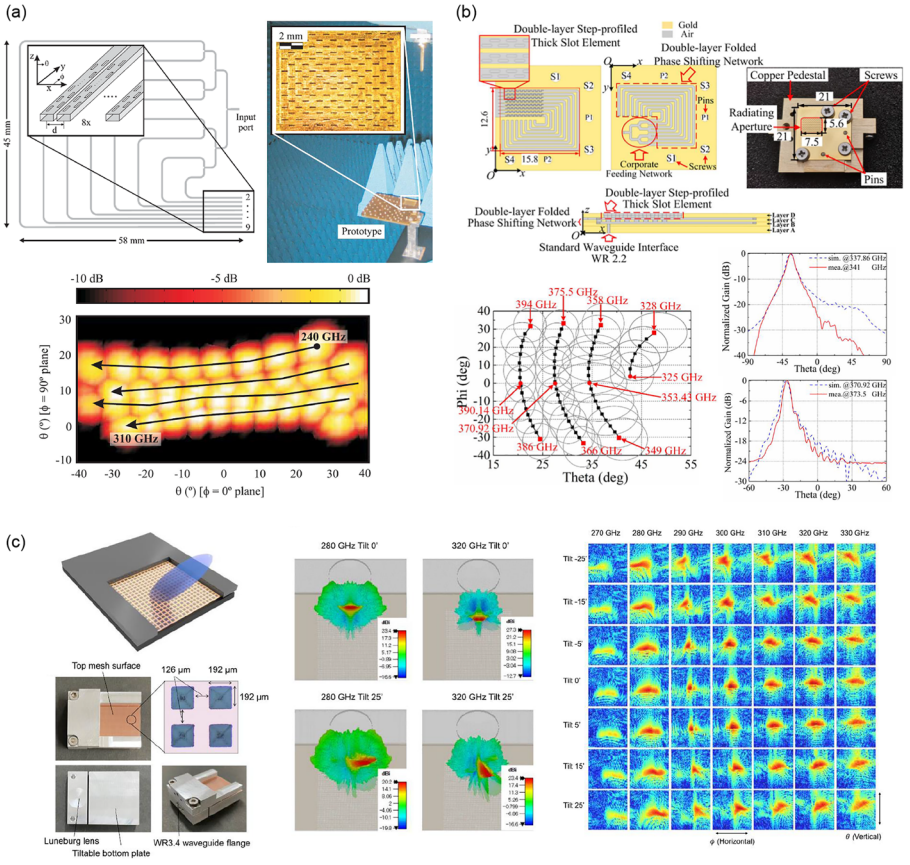

Fig. 21 **a** Hybrid combination of parallel and serial array enabling 2D frequency scanning [163]. Copyright 2017, IEEE. **b** Footprint-compressed hybrid parallel and serial array for 2D frequency scanning [164]. Copyright 2021, IEEE. **c** 2D leaky-wave antenna based on controllable internal trajectory. Vertical steering by frequency sweep and horizontal steering by minute plate tilt can be combined [165]. Copyright 2021, IEEE

horizontally by a small tilt of the plate. Although it requires mechanical movement, a small tilt can involve large deflection via a graded refractive index. An experimental result shows vertical steering over 15° by sweeping the frequency from 270 to 330 GHz and horizontal steering over 20° by tilting the plate from −0.42 to +0.42°.

5 Application-Driven System Designs

As we have reviewed in this article, THz beam steering has been considered in a variety of approaches based on active and passive phased arrays, variable lenses, gratings, metasurfaces, and leaky-wave antennas. However, each has its specific challenges, and a definitive method has yet to be established. Meanwhile, practical THz applications cannot evolve without beam steering. Based on this situation, application-driven system design approaches that implement beam steering effectively for a specific purpose, rather than necessarily pursuing versatility, using limited hardware resources have been emerging recently. Such an approach is valuable, particularly at the dawn of the THz technologies.

5.1 Adaptive Alignment in Wireless Communication

Owing to the broad bandwidth, the use of THz waves for wireless communication is becoming a hot topic. The distinct feature of THz waves as compared to the low-frequency counterparts is that highly directional links are indispensable as discussed in Section 1. Consequently, frequent alignment between a transmitter and a receiver is required to compensate for the misalignment due to the movement of devices and also the change of the channel properties. The alignment can be achieved in both the physical layer (devices) and the protocol layer (design of the preambles). In the physical layer, brute-force search of the best beamforming combination between the transmitter and the receiver has a complexity of $O(N^2)$, where N is the total number of beam directions configurable for each antenna. By carefully designing the localization strategy, this can be reduced to $O(K \log N)$, where K is the number of paths

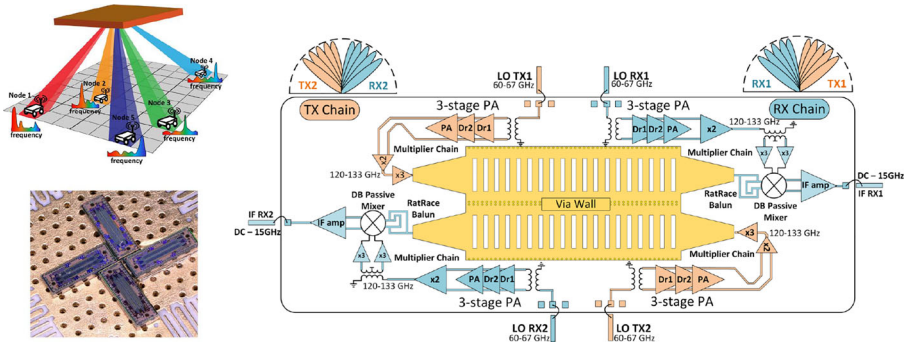

Fig. 22 Leaky-wave THz antennas and transceivers in CMOS for one-shot simultaneous localization of multiple wireless nodes [166]. Creative Commons Attribution (CC BY) license

traveled by the signal in each hashing [167]. It can significantly reduce the cost of beamforming when combined with a preamble design with callbacks that contain channel information. Signal path planning based on Digital Twin has also been proposed, which predicts indoor signal propagation characteristics to be controlled with tunable metamaterial walls [168].

One approach to implement such a physical layer is to use a leaky-wave antenna with spectrum-to-space mapping capability as discussed in Section 4.

Saeidi et al. have developed an on-chip leaky-wave antenna system that covers $\pm$ 40° using a frequency bandwidth of 40 GHz from 360 to 400 GHz and attains a 1D localization accuracy of 1° with a 200-Hz bandwidth and a 2D localization accuracy of 2° with a 20-Hz bandwidth [166, 169]. The leaky-wave antenna is fed with frequency multipliers that multiply a seed frequency six-fold as illustrated in Fig. 22. A mixer-first topology involves a large noise figure of 26.2 dB. Ma et al. have exploited a leaky waveguide to allow frequency-dependent directional transmission [170]. Two channels with center frequencies at 264.7 GHz and 332.5 GHz are used simultaneously for data transmission with an aggregate data rate of 50 Gbps. Another demonstration of the frequency-dependant beam property of leaky-wave antennas has been presented in [171], in which the leaky-wave antenna is used for one-shot localization with an error of a few degrees. Lu et al. have demonstrated photonic beam steering combined with a leaky-wave antenna [146]. The proposed approach allows THz beam steering from 6 to 39° by varying the beat frequency from 280 to 330 GHz at a speed of up to 28°/s based on an optical heterodyne system. A data rate of 24 Gbps is achieved for a single user for all beam directions and at short wireless distances up to 6 cm has been demonstrated without using a THz amplifier in the transmitter chip.

5.2 Fast Scanning for Sensing and Imaging

Imaging with THz waves has great potentials for scientific, medical, and industrial applications [173]. Although a massive array of sensitive detectors, i.e., a low-frequency counterpart of a camera, is yet to be available in the THz range, beam steering enables spatially resolved data acquisition with a limited number of detectors. To overcome the lack of complete phased arrays, the use of frequency scanning, in which angular information can be mapped to spectral information, has been considered. For example, by transmitting and receiving broadband signals with a grating, a line image can be extracted from spectral analysis of the signal. Both sequential frequency sweep and short pulse transmission can be considered for this approach. Schumann et al. have demonstrated 2D imaging by repeating such 1D scans line-by-line using a THz time-domain spectroscopy system [174]. An image consisting of 240 lines can be obtained with a scan rate of 12 Hz and a total acquisition time of 20 s. In addition to the lateral 2D imaging, coverage into the other dimension is also possible, i.e., a range-angle image can be extracted. Li et al. have combined range and angle estimation based on matched filtering and multiple signal classification to analyze signals acquired with a grating [175]. Two metal rods placed at a distance of 0.3 m can be precisely located.

The experimental systems for frequency scanning as above are based on diffraction gratings. When using a grating, plane-wave incidence implemented with a spatial optics is required as a feeding system. Such a volumetric system, however, can be integrated into a planar system by using a leaky-wave antenna reviewed in Section 4.2. For example, the microstrip periodic leaky-wave antenna [143] mentioned in Section 4.2.1 has been shown to serve as radar enabling range-angle map acquisition. When a target is placed in front of the radar, the peak frequency of the received spectrum and the peak time of its Fourier transform are associated with the angle and range towards the target, respectively. If such radar is arrayed, or equivalently it is moved so that aperture-synthesis is allowed, 3D imaging can also be attained [176]. In addition to the sequential frequency sweep, broadband pulse transmission can be used for this approach. While the former allows high signal purity at the cost of sweep time, the latter enables simultaneous data acquisition advantageous for high-speed operation [177]. Although the above demonstrations have relied on a vector network analyzer or a femtosecond pulse laser to transmit and receive THz waves, a standalone palmtop THz radar system composed of a leaky-wave antenna incorporating a frequency multiplier and SBDs has been demonstrated [172]. To enable beam steering and homodyne detection in one package without a duplexer, a pair of reverse-connected leaky-wave antennas (i.e., a center-fed leaky-wave antenna) shown in Fig. 23 has been developed. Using this system, a demonstration of human heartbeat monitoring through the clothes has been presented by detecting phase difference between two successive inverse Fourier transform frames at every 30 ms.

It should be emphasized that integrated circuits for THz radar have been developing substantially in recent years [180]. There, one of the key factors is to develop an antenna system that ensures TX-RX isolation because practical circulators are still unavailable. J. Grzyb et al. have developed monostatic FMCW radar based on a circularly polarized antenna capable of separating left- and right-handed circularly polarized waves integrated with a SiGe HBT chip operating at 210–270 GHz [181].

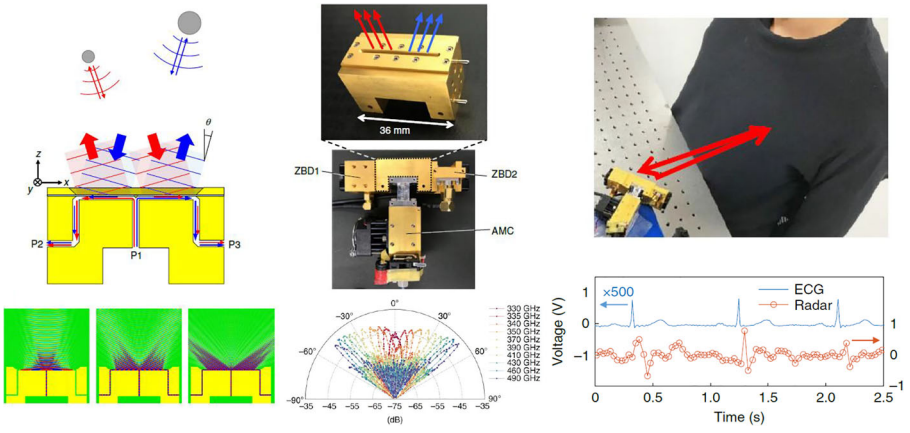

Fig. 23 Integrated THz radar based on leaky-wave coherence tomography [172]. Copyright 2020, Springer Nature

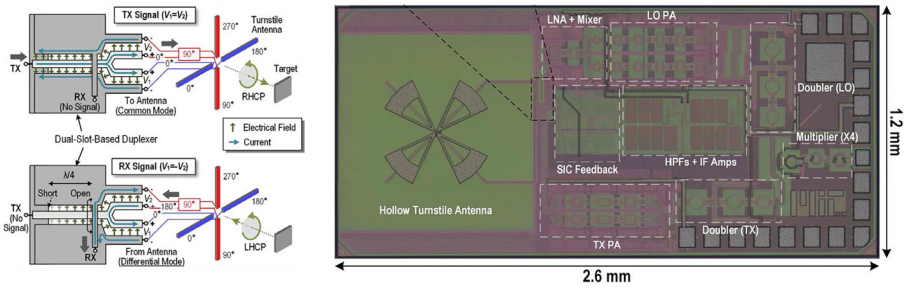

Fig. 24 Integrated turnstile antenna with polarization selective coupler for 140 GHz FMCW radar [178]. Copyright 2022, IEEE

In addition to the attained TX-RX isolation of 26 dB, the approach is advantageous in suppressing ghosts and jamming. Chen et al. have developed CMOS on-chip monostatic FMCW radar at 140 GHz that attains TX-RX isolation of 33.3 dB for circularly polarized waves using a turnstile antenna with a dual-slot-based duplexer as shown in Fig. 24 [178]. Naghavi et al. have developed an autodyne FMCW radar at 250 GHz based on BiCMOS technology [182]. Monostatic configuration is readily available in this approach since the autodyne oscillator simultaneously carries out functions of generating signals to be transmitted and mixing the transmitted and reflected signals. Besides, the quasi-optically implemented phase processing can resolve sub-wavelength displacements. To enhance the phase measurement quality, Simic et al. have developed a two-step IQ down-conversion RX architecture at 420 GHz based on 40 nm CMOS technology that attains RMS accuracy of 2.8° and RMS 1σ of 1.7° [183]. Although demonstrated in a back-to-back transmission configuration, it could be extended into a reflection configuration. Another attempt of expanding the bandwidth for higher range resolution has been presented by Yi et al. in Fig. 25, where multiple on-chip antennas are placed in an array configuration based on 65 nm CMOS technology, which altogether achieves an aggregate bandwidth of 100 GHz from 220 to 320 GHz [179]. Developing beam steering on those emerging integrated THz circuits will be an important research direction.

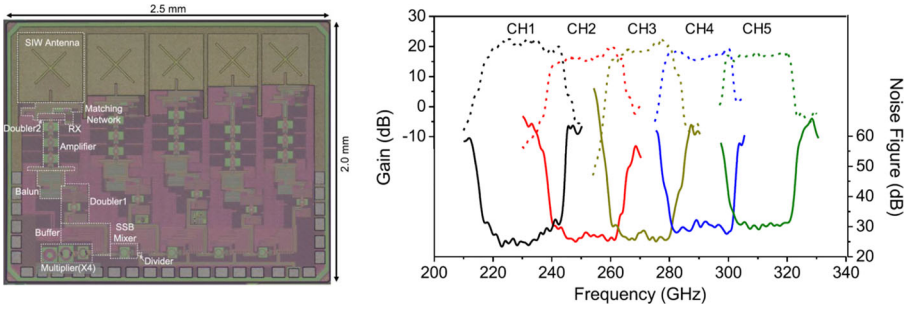

Fig. 25 Integrated FMCW radar with 100 GHz bandwidth implemented by combining an array of patch antennas working across the frequency of interest. The cross patterns on the antenna are designed to introduce more modes to increase the bandwidth [179]. Copyright 2021, IEEE

6 Conclusion and Future Outlook

Owing to the broad bandwidth and high spatial resolution, THz communication and sensing will be a key technology for interfacing physical and cyber worlds in the 6G era and beyond. Wireless transmission of the THz waves necessitates directional beams to mitigate severe diffraction losses due to the shorter wavelengths than that of the microwaves. Therefore, the implementation of THz beam steering becomes indispensable. In this article, we have reviewed the techniques and challenges to implement THz beam steering.

The use of phased arrays reviewed in Section 2 is the fundamental approach to beam steering. The active phased arrays demonstrated so far are composed of a small number of oscillators arrayed in a millimeter-scale area. However, to transmit THz waves over a distance of meters, a centimeter-scale array is required as discussed in Section 1. In addition, the spacing between adjacent radiation elements must be no larger than the half-wavelength to suppress grating lobes. There are ongoing research efforts for fully digital arrays particularly in the lower sub-THz bands. The use of photonics-based approaches is also considered. To implement high density and massive arrays, the number of radiation elements must be increased by several orders of magnitude. The passive phased arrays composed of a single transmitter connected to a large-scale phase shifter network could mitigate this challenge. The use of passive structures is also advantageous in terms of compatibility with high-power amplifiers and reversibility of transmission and reception. However, the implementation of low-loss and broadband THz phase shifters remains as another unresolved issue.

Along with the efforts to develop the THz phased arrays, the use of reconfigurable diffraction in which wave generation and wavefront manipulation are decoupled has been considered as low-cost alternatives. Such an approach is implemented with variable structures as reviewed in Section 3 and frequency sweeping in Section 4. However, as with the implementation of phase shifters, the use of variable materials such as liquid crystals is associated with high losses. The use of MEMS could offer lower losses at the cost of the operation speed. Considering a scenario of THz beam tracking to and from mobile/wearable devices, the beam steering speed must be much faster than that of the mobility of the receiver. The requirement will be even higher when considering time-division multiplexing of multiple devices. Electronically programmable impedance surfaces are promising for such high-speed operation although further reduction of the losses is required. The use of frequency sweeping based on dispersive structures for beam steering also has a potential of high-speed operation, but it limits the spectral bandwidth in each direction. In addition, bilateral use of this approach will be limited because linking between two such antennas on a transmitter and a receiver requests the two antennas to be aligned in the specific mutual orientation. On the other hand, the inherent spectral decomposition function can be used for physical layer signal processing.

We summarize the demonstrated beam steering range in Fig. 26 for the representative approaches reviewed in this article. Beam steering using electronic phased arrays has mainly been developed below 400 GHz while photonic phased arrays can operate at higher frequencies. Wide range 2D beam steering can be attained with H-tree

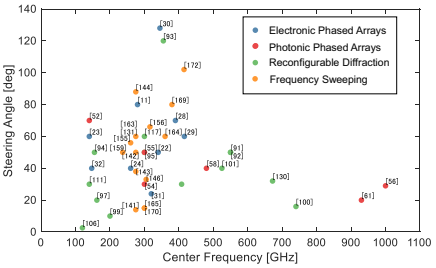

Approach	Principle	Device	Representative examples and features
Electronic Phased Array	Phase shifters / Coupled oscillation	CMOS, SiGe	2D steerable arrays [11], [22], [29], [30], [32], T/R bi-directional steering [24], [32], High power (~ 28 dBm) steering [23], Wide range steering (128°×53°) [30], Receiver steering [52]
Photonic Phased Array	Phase shifted optical pumping	Photoconductive antennas, UTC-PD	Spatially modulated femtosecond laser pumping [54], [55], [58], Fiber integrated optical pumping [56], [61]
Reconfigurable Diffraction	Variable structures	Lenses, Gratings	Movable lenses [91], [92], Luneburg lenses [93], [94], [97], Variable effective index [95], Photo-induced carriers [99], [100], Transformable gratings [101], [106], [111], CMOS-based grating [117], Liquid crystal-based grating [130], [131]
Frequency Scanning	Variable frequency	Leaky-wave antennas, Gratings	2D steerable structures [142], [163-165], Microstrip LWA [143], [144], [146], Wide aperture [155], Backward enabled [159], Slotted parallel plate [156], [170], Paired LWAs [169], [172]

Fig. 26 Summary of the demonstrated beam steering ranges for the representative approaches reviewed in this article

based CMOS oscillators (80° × 80°) [11] and standing-wave coupled SiGe oscillators (128° × 53°) [30]. When using reconfigurable diffractive structures, wide range steering is obtained with a Luneburg lens [93] although it is discrete beam switching relying on port switching. Apart from that, the use of a CMOS-based reconfigurable metasurface allows wide range steering [117]. Both active and passive arrays have a common problem of scan blindness [184, 185]: if the beam tilt increases, non-radiative surface waves are excited through coupling between adjacent radiation elements on the substrate. In the microwave range, attempts to mitigate the scan blindness by decoupling adjacent elements via artificial surfaces have been considered [186, 187] and implemented recently in a large-scale array [188, 189]. Similar approaches will be required for the THz range although additional losses associated with such artificial surfaces must be avoided. Meanwhile, the frequency sweeping of leaky-waves, i.e., radiative surface waves, is suited for beam steering towards horizontal directions. However, the radiation efficiency of leaky-wave antennas towards broadside directions is rather suppressed. A center-fed leaky-wave antenna can generate symmetric beams, thereby doubling the beam coverage [172]. 2D beam steering is also allowed by optimizing the feeding network [163, 164].

Thus, effective and efficient THz beam steering and array architecture is still an open challenge. While this review article focuses on beam steering, its combination with dynamic polarization control [190–192] will be another challenge that is important for tracking mobile/wearable devices. Addressing these challenges might require a multi-disciplinary effort utilizing concepts across various disciplines including materials, antenna, metasurface and subwavelength electromagnetics, RFICs, photonics, and MEMS. In addition, by blurring across the various levels of abstraction, new THz architectures can emerge that might look very different from traditional approaches but have functionalities not realizable otherwise [45]. Novel beam-steering mechanisms including spatial-temporal modulation have also been proposed that may further enhance the efficiency of THz beamforming while facilitating applications such as radar and secure wireless communication [172, 193–195]. Regardless of the steering mechanisms, structural optimization for extending the steerable range and operation bandwidth will be important. Such optimization can be performed based on computational approaches including topology optimization [196], inverse design [197], and deep learning [198] as has been applied to RFICs and photonics. In

contrast to photonics, in which the structures are dielectric-based, the use of metals should also be considered explicitly in the THz range [199]. On top of the structural optimization of a single device, system-level optimization to overcome the limitation of a single device will play an important role. This includes a discussion on how to integrate multiple beam steering antennas to attain wide coverage, in which the required specification depends on applications. Thus, such discussions should be application-driven and should keep pace with the development of fundamental THz devices.

Author Contribution All of the authors contributed to writing the manuscript.

Funding Open access funding provided by University of Tokyo. YM would like to acknowledge funding organizations including Japan Society for the Promotion of Science 20H02154, Japan Science and Technology Agency JPMJPR18J9, Ministry of Internal Affairs and Communications 165103002, and National Institute of Information and Communications Technology 06101. KS would like to acknowledge funding organizations such as the National Science Foundation, Defense Advanced Research Program Agency, Office of Naval Research, Army Research Office, and Air Force Office of Scientific Research, and GlobalFoundries for foundry support.

Availability of Data and Materials Not applicable.

Declarations

Ethics Approval Not applicable.

Conflict of Interest The authors declare no competing interests.

References

1. C. A. Balanis, *Modern antenna handbook*. John Wiley and Sons, 2011.
2. T. Nagatsuma, G. Ducournau, and C. C. Renaud, "Advances in terahertz communications accelerated by photonics," *Nature Photonics*, vol. 10, no. 6, pp. 371–379, 2016.
3. D. Headland, Y. Monnai, D. Abbott, C. Fumeaux, and W. Withayachumnankul, "Tutorial: Terahertz beamforming, from concepts to realizations," *Apl Photonics*, vol. 3, no. 5, p. 051101, 2018.
4. X. Fu, F. Yang, C. Liu, X. Wu, and T. J. Cui, "Terahertz beam steering technologies: From phased arrays to field-programmable metasurfaces," *Advanced optical materials*, vol. 8, no. 3, p. 1900628, 2020.
5. K. Sengupta, T. Nagatsuma, and D. M. Mittleman, "Terahertz integrated electronic and hybrid electronic–photonic systems," *Nature Electronics*, vol. 1, no. 12, pp. 622–635, 2018.
6. K. Sengupta, "Integrated circuits for terahertz communication beyond 100 ghz: Are we there yet?" in *2019 IEEE International Conference on Communications Workshops (ICC Workshops)*. IEEE, 2019, pp. 1–6.

7. K. Delfanazari, R. A. Klemm, H. J. Joyce, D. A. Ritchie, and K. Kadowaki, "Integrated, portable, tunable, and coherent terahertz sources and sensitive detectors based on layered superconductors," *Proceedings of the IEEE*, vol. 108, no. 5, pp. 721–734, 2020.
8. A. Arabhavi, F. Ciabattini, S. Hamzeloui, R. Flückiger, T. Popovic, D. Han, D. Marti, G. Bonomo, R. Chaudhary, O. Ostinelli, and C. Bolognesi, "InP/GaAsSb double heterojunction bipolar transistor technology with f_{MAX} = 1.2 THz," in *2021 IEEE International Electron Devices Meeting (IEDM)*, 2021, pp. 11.4.1–11.4.4.
9. D. Huang, T. R. LaRocca, M.-C. F. Chang, L. Samoska, A. Fung, R. L. Campbell, and M. Andrews, "Terahertz CMOS frequency generator using linear superposition technique," *IEEE Journal of Solid-State Circuits*, vol. 43, no. 12, pp. 2730–2738, 2008.
10. E. Seok, C. Cao, D. Shim, D. J. Arenas, D. B. Tanner, C.-M. Hung, and K. O. Kenneth, "A 410GHz CMOS push-push oscillator with an on-chip patch antenna," in *2008 IEEE International Solid-State Circuits Conference - Digest of Technical Papers*, 2008, pp. 472–629.
11. K. Sengupta and A. Hajimiri, "A 0.28 THz power-generation and beam-steering array in CMOS based on distributed active radiators," *IEEE Journal of Solid-State Circuits*, vol. 47, no. 12, pp. 3013–3031, 2012.
12. K. Sengupta and A. Hajimiri, "Distributed active radiation for thz signal generation," in *2011 IEEE International Solid-State Circuits Conference*. IEEE, 2011, pp. 288–289.
13. K. Sengupta and A. Hajimiri, "A 0.28 thz 4× 4 power-generation and beam-steering array," in *2012 IEEE International Solid-State Circuits Conference*. IEEE, 2012, pp. 256–258.
14. Z. Ahmad, M. Lee, and K. O. Kenneth, "20.5 1.4THz, -13dBm-EIRP frequency multiplier chain using symmetric- and asymmetric-cv varactors in 65nm CMOS," *2016 IEEE International Solid-State Circuits Conference (ISSCC)*, pp. 350–351, 2016.
15. Z. Hu, M. Kaynak, and R. Han, "High-power radiation at 1 THz in silicon: A fully scalable array using a multi-functional radiating mesh structure," *IEEE Journal of Solid-State Circuits*, vol. 53, no. 5, pp. 1313–1327, 2018.
16. U. R. Pfeiffer, Y. Zhao, J. Grzyb, R. A. Hadi, N. Sarmah, W. Förster, H. Rücker, and B. Heinemann, "14.5 a 0.53THz reconfigurable source array with up to 1mw radiated power for terahertz imaging applications in 0.13μm SiGe biCMOS," in *2014 IEEE International Solid-State Circuits Conference Digest of Technical Papers (ISSCC)*, 2014, pp. 256–257.
17. R. Izumi, S. Suzuki, and M. Asada, "1.98 thz resonant-tunneling-diode oscillator with reduced conduction loss by thick antenna electrode," in *2017 42nd International Conference on Infrared, Millimeter, and Terahertz Waves (IRMMW-THz)*. IEEE, 2017, pp. 1–2.
18. Y. Suzuki, T. Van Mai, X. Yu, S. Suzuki, and M. Asada, "Phase control of terahertz waves using injection-locked resonant tunneling diode oscillator," *IEEE Transactions on Terahertz Science and Technology*, 2022.
19. Y.-Y. Li, J.-Q. Liu, F.-Q. Liu, J.-C. Zhang, S.-Q. Zhai, N. Zhuo, L.-J. Wang, S.-M. Liu, and Z.-G. Wang, "High power-efficiency terahertz quantum cascade laser," *Chinese Physics B*, vol. 25, no. 8, p. 084206, 2016.
20. T.-Y. Kao, Q. Hu, and J. L. Reno, "Phase-locked arrays of surface-emitting terahertz quantum-cascade lasers," *Applied Physics Letters*, vol. 96, no. 10, p. 101106, 2010.
21. C. Gaolei, Z. Huan, Y. Chenren, Z. Haiqing, X. Gangyi, and H. Li, "Phase-locked pair of terahertz quantum cascade lasers through evanescent-wave coupling," *Infrared Physics & Technology*, vol. 109, p. 103427, 2020.
22. Y. Tousi and E. Afshari, "A high-power and scalable 2-d phased array for terahertz CMOS integrated systems," *IEEE Journal of Solid-State Circuits*, vol. 50, no. 2, pp. 597–609, 2015.
23. S. Li, Z. Zhang, B. Rupakula, and G. M. Rebeiz, "An eight-element 140 GHz wafer-scale phased-array transmitter with 32 dBm peak EIRP and > 16 Gbps 16QAM and 64QAM operation," in *2021 IEEE MTT-S International Microwave Symposium (IMS)*, 2021, pp. 795–798.
24. I. Abdo, C. d. Gomez, C. Wang, K. Hatano, Q. Li, C. Liu, K. Yanagisawa, A. A. Fadila, J. Pang, H. Hamada, H. Nosaka, A. Shirane, and K. Okada, "22.2 a 300GHz-band phased-array transceiver using bi-directional outphasing and hartley architecture in 65nm CMOS," in *2021 IEEE International Solid- State Circuits Conference (ISSCC)*, vol. 64, 2021, pp. 316–318.
25. H. Saeidi, S. Venkatesh, C. R. Chappidi, T. Sharma, C. Zhu, and K. Sengupta, "29.9 a 4×4 distributed multi-layer oscillator network for harmonic injection and THz beamforming with 14dBm EIRP at 416GHz in a lensless 65nm CMOS IC," in *2020 IEEE International Solid-State Circuits Conference-(ISSCC)*. IEEE, 2020, pp. 256–258.

26. K. Sengupta and A. Hajimiri, "Mutual synchronization for power generation and beam-steering in CMOS with on-chip sense antennas near 200 GHz," *IEEE Transactions on Microwave Theory and Techniques*, vol. 63, no. 9, pp. 2867–2876, 2015.
27. K. Sengupta and A. Hajimiri, "Designing optimal surface currents for efficient on-chip mm-wave radiators with active circuitry," *IEEE Transactions on Microwave Theory and Techniques*, vol. 64, no. 7, pp. 1976–1988, 2016.
28. Y. Yang, O. D. Gurbuz, and G. M. Rebeiz, "An eight-element 370–410-GHz phased-array transmitter in 45-nm CMOS SOI with peak EIRP of 8–8.5 dBm," *IEEE Transactions on Microwave Theory and Techniques*, vol. 64, no. 12, pp. 4241–4249, 2016.
29. H. Saeidi, S. Venkatesh, C. R. Chappidi, T. Sharma, C. Zhu, and K. Sengupta, "A 4×4 steerable 14 dbm eirp array on cmos at 0.41 thz with a 2d distributed oscillator network," *IEEE Journal of Solid-State Circuits*, 2022.
30. H. Jalili and O. Momeni, "17.10 a 318-to-370GHz standing-wave 2D phased array in 0.13μm biCMOS," in *2017 IEEE International Solid-State Circuits Conference (ISSCC)*, 2017, pp. 310–311.
31. X. Deng, Y. Li, J. Li, C. Liu, W. Wu, and Y. Xiong, "A 320-GHz 1×4 fully integrated phased array transmitter using 0.13-μm SiGe biCMOS technology," *IEEE Transactions on Terahertz Science and Technology*, vol. 5, no. 6, pp. 930–940, 2015.
32. M. Elkhouly, J. Ha, M. J. Holyoak, D. Hendry, M. Sayginer, R. Enright, I. Kimionis, Y. Baeyens, and S. Shahramian, "Fully integrated 2D scalable Tx/Rx chipset for D-band phased-array-on-glass modules," in *2022 IEEE International Solid- State Circuits Conference (ISSCC)*, vol. 65, 2022, pp. 76–78.
33. M. M. Assefzadeh and A. Babakhani, "Broadband 0.03–1.032 THz signal generation and radiation based on a fully-integrated 4× 2 impulse radiating array in 90nm SiGe biCMOS," in *2016 41st International Conference on Infrared, Millimeter, and Terahertz waves (IRMMW-THz)*. IEEE, 2016, pp. 1–2.
34. M. M. Assefzadeh and A. Babakhani, "A fully-integrated digitally-programmable 4× 4 picosecond digital-to-impulse radiating array in 65 nm bulk CMOS," in *2016 IEEE MTT-S International Microwave Symposium (IMS)*. IEEE, 2016, pp. 1–4.
35. X. Wu and K. Sengupta, "Dynamic waveform shaping for reconfigurable radiated periodic signal generation with picosecond time-widths," in *2015 IEEE Custom Integrated Circuits Conference (CICC)*. IEEE, 2015, pp. 1–4.
36. X. Wu and K. Sengupta, "Dynamic waveform shaping with picosecond time widths," *IEEE Journal of Solid-State Circuits*, vol. 52, no. 2, pp. 389–405, 2016.
37. X. Wu and K. Sengupta, "Programmable picosecond pulse generator in cmos," in *2015 IEEE MTT-S International Microwave Symposium*. IEEE, 2015, pp. 1–4.
38. O. Ajakaiye, J. Grade, C. Shin, and T. Kenny, "Wafer-scale fabrication of infrared detectors based on tunneling displacement transducers," *Sensors and Actuators A: Physical*, vol. 134, no. 2, pp. 575–581, 2007.
39. A. Kuzmin, S. Doerner, S. Singer, I. Charaev, K. Ilin, S. Wuensch, and M. Siegel, "Terahertz transition-edge sensor with kinetic-inductance amplifier at 4.2 k," *IEEE Transactions on Terahertz Science and Technology*, vol. 8, no. 6, pp. 622–629, 2018.
40. A. El Fatimy, R. L. Myers-Ward, A. K. Boyd, K. M. Daniels, D. K. Gaskill, and P. Barbara, "Epitaxial graphene quantum dots for high-performance terahertz bolometers," *Nature nanotechnology*, vol. 11, no. 4, pp. 335–338, 2016.
41. Z.-y. Liu, L.-y. Liu, J. Yang, and N.-j. Wu, "A CMOS fully integrated 860-GHz terahertz sensor," *IEEE Transactions on Terahertz Science and Technology*, vol. 7, no. 4, pp. 455–465, 2017.
42. M. Ali and M. Perenzoni, "A readout channel optimized for minimum NEP of a FET-based THz pixel," *Journal of Infrared, Millimeter, and Terahertz Waves*, vol. 39, no. 12, pp. 1221–1235, 2018.
43. K. Sengupta, D. Seo, L. Yang, and A. Hajimiri, "Silicon integrated 280 GHz imaging chipset with 4×4 SiGe receiver array and CMOS source," *IEEE Transactions on Terahertz Science and Technology*, vol. 5, no. 3, pp. 427–437, 2015.
44. T. J. Smith, A. Broome, D. Stanley, J. Westberg, G. Wysocki, and K. Sengupta, "A hybrid thz imaging system with a 100-pixel cmos imager and a 3.25–3.50 thz quantum cascade laser frequency comb," in *ESSCIRC 2019-IEEE 45th European Solid State Circuits Conference (ESSCIRC)*. IEEE, 2019, pp. 151–154.

45. X. Wu, H. Lu, and K. Sengupta, "Programmable terahertz chip-scale sensing interface with direct digital reconfiguration at sub-wavelength scales," *Nature communications*, vol. 10, no. 1, pp. 1–13, 2019.
46. Z. Hu, C. Wang, and R. Han, "A 32-unit 240-GHz heterodyne receiver array in 65-nm CMOS with array-wide phase locking," *IEEE Journal of Solid-State Circuits*, vol. 54, no. 5, pp. 1216–1227, 2019.
47. X. Lu, C. R. Chappidi, X. Wu, and K. Sengupta, "Antenna preprocessing and element-pattern shaping for multi-band mmwave arrays: Multi-port receivers and antennas," *IEEE Journal of Solid-State Circuits*, vol. 55, no. 6, pp. 1455–1470, 2020.
48. C. R. Chappidi, X. Lu, X. Wu, and K. Sengupta, "Antenna preprocessing and element-pattern shaping for multi-band mmwave arrays: Multi-port transmitters and antennas," *IEEE Journal of Solid-State Circuits*, vol. 55, no. 6, pp. 1441–1454, 2020.
49. X. Lu, X. Wu, H. Saeidi, and K. Sengupta, "A multi-port dual polarized antenna coupled mm-wave CMOS receiver with element-level pattern and notch programmability and passive interferer rejection capability," in *2019 IEEE Custom Integrated Circuits Conference (CICC)*, 2019, pp. 1–4.
50. X. Wu and K. Sengupta, "On-chip THz spectroscope exploiting electromagnetic scattering with multi-port antenna," *IEEE Journal of Solid-State Circuits*, vol. 51, no. 12, pp. 3049–3062, 2016.
51. X. Wu and K. Sengupta, "25.3 a 40-to-330ghz synthesizer-free thz spectroscope-on-chip exploiting electromagnetic scattering," in *2016 IEEE International Solid-State Circuits Conference (ISSCC)*. IEEE, 2016, pp. 428–429.
52. S. Li, Z. Zhang, B. Rupakula, and G. M. Rebeiz, "An eight-element 140-GHz wafer-scale if beamforming phased-array receiver with 64-qam operation in CMOS RFSOI," *IEEE Journal of Solid-State Circuits*.
53. U. R. Pfeiffer, R. Jain, J. Grzyb, S. Malz, P. Hillger, and P. Rodríguez-Vízquez, "Current status of terahertz integrated circuits-from components to systems," in *2018 IEEE BiCMOS and Compound Semiconductor Integrated Circuits and Technology Symposium (BCICTS)*. IEEE, 2018, pp. 1–7.
54. N. M. Froberg, B. B. Hu, X.-C. Zhang, and D. H. Auston, "Terahertz radiation from a photoconducting antenna array," *IEEE Journal of Quantum Electronics*, vol. 28, no. 10, pp. 2291–2301, 1992.
55. K.-i. Maki and C. Otani, "Terahertz beam steering and frequency tuning by using the spatial dispersion of ultrafast laser pulses," *Optics Express*, vol. 16, no. 14, pp. 10158–10169, 2008.
56. M. Che, Y. Matsuo, H. Kanaya, H. Ito, T. Ishibashi, and K. Kato, "Optoelectronic thz-wave beam steering by arrayed photomixers with integrated antennas," *IEEE Photonics Technology Letters*, vol. 32, no. 16, pp. 979–982, 2020.
57. B. B. Hu, J. T. Darrow, X.-C. Zhang, D. H. Auston, and P. R. Smith, "Optically steerable photoconducting antennas," *Applied physics letters*, vol. 56, no. 10, pp. 886–888, 1990.
58. K. Uematsu, K.-i. Maki, and C. Otani, "Terahertz beam steering using interference of femtosecond optical pulses," *Optics Express*, vol. 20, no. 20, pp. 22914–22921, 2012.
59. P. Lu, M. Steeg, K. Kolpatzeck, S. Dülme, B. Khani, A. Czylwik, and A. Stöhr, "Photonic assisted beam steering for millimeter-wave and THz antennas," in *2018 IEEE Conference on Antenna Measurements & Applications (CAMA)*. IEEE, 2018, pp. 1–4.
60. C. McDonnell, J. Deng, S. Sideris, G. Li, and T. Ellenbogen, "Terahertz metagrating emitters with beam steering and full linear polarization control," *Nano Letters*, vol. 22, no. 7, pp. 2603–2610, 2022.
61. M. Che, K. Kondo, H. Kanaya, and K. Kato, "Arrayed photomixers for thz beam-combining and beam-steering," *Journal of Lightwave Technology*, 2022.
62. H.-T. Chen, W. J. Padilla, M. J. Cich, A. K. Azad, R. D. Averitt, and A. J. Taylor, "A metamaterial solid-state terahertz phase modulator," *Nature photonics*, vol. 3, no. 3, pp. 148–151, 2009.
63. S. H. Lee, M. Choi, T.-T. Kim, S. Lee, M. Liu, X. Yin, H. K. Choi, S. S. Lee, C.-G. Choi, S.-Y. Choi *et al.*, "Switching terahertz waves with gate-controlled active graphene metamaterials," *Nature materials*, vol. 11, no. 11, pp. 936–941, 2012.
64. Y. Zhao, Y. Zhang, Q. Shi, S. Liang, W. Huang, W. Kou, and Z. Yang, "Dynamic photoinduced controlling of the large phase shift of terahertz waves via vanadium dioxide coupling nanostructures," *ACS Photonics*, vol. 5, no. 8, pp. 3040–3050, 2018.
65. H. Zeng, H. Liang, Y. Zhang, L. Wang, S. Liang, S. Gong, Z. Li, Z. Yang, X. Zhang, F. Lan *et al.*, "High-precision digital terahertz phase manipulation within a multichannel field perturbation coding chip," *Nature Photonics*, vol. 15, no. 10, pp. 751–757, 2021.

66. Y. Urade, Y. Nakata, K. Okimura, T. Nakanishi, F. Miyamaru, M. W. Takeda, and M. Kitano, "Dynamically babinet-invertible metasurface: a capacitive-inductive reconfigurable filter for terahertz waves using vanadium-dioxide metal-insulator transition," *Optics express*, vol. 24, no. 5, pp. 4405–4410, 2016.
67. P.-Y. Chen, C. Argyropoulos, and A. Alu, "Terahertz antenna phase shifters using integrally-gated graphene transmission-lines," *IEEE Transactions on Antennas and Propagation*, vol. 61, no. 4, pp. 1528–1537, 2012.
68. C.-S. Yang, T.-T. Tang, R.-P. Pan, P. Yu, and C.-L. Pan, "Liquid crystal terahertz phase shifters with functional indium-tin-oxide nanostructures for biasing and alignment," *Applied Physics Letters*, vol. 104, no. 14, p. 141106, 2014.
69. J. Yang, C. Cai, Z. Yin, T. Xia, S. Jing, H. Lu, and G. Deng, "Reflective liquid crystal terahertz phase shifter with tuning range of over 360°," *IET Microwaves, Antennas & Propagation*, vol. 12, no. 9, pp. 1466–1469, 2018.
70. B. S.-Y. Ung, X. Liu, E. P. Parrott, A. K. Srivastava, H. Park, V. G. Chigrinov, and E. Pickwell-MacPherson, "Towards a rapid terahertz liquid crystal phase shifter: Terahertz in-plane and terahertz out-plane (tip-top) switching," *IEEE Transactions on Terahertz Science and Technology*, vol. 8, no. 2, pp. 209–214, 2018.
71. N. Vieweg, C. Jansen, M. K. Shakfa, M. Scheller, N. Krumbholz, R. Wilk, M. Mikulics, and M. Koch, "Molecular properties of liquid crystals in the terahertz frequency range," *Optics express*, vol. 18, no. 6, pp. 6097–6107, 2010.
72. H. Park, E. P. Parrott, F. Fan, M. Lim, H. Han, V. G. Chigrinov, and E. Pickwell-MacPherson, "Evaluating liquid crystal properties for use in terahertz devices," *Optics express*, vol. 20, no. 11, pp. 11899–11905, 2012.
73. M. Reuter, N. Vieweg, B. Fischer, M. Mikulicz, M. Koch, K. Garbat, and R. Dabrowski, "Highly birefringent, low-loss liquid crystals for terahertz applications," *APL materials*, vol. 1, no. 1, p. 012107, 2013.
74. C.-Y. Chen, T.-R. Tsai, C.-L. Pan, and R.-P. Pan, "Room temperature terahertz phase shifter based on magnetically controlled birefringence in liquid crystals," *Applied physics letters*, vol. 83, no. 22, pp. 4497–4499, 2003.
75. T.-R. Tsai, C.-Y. Chen, R.-P. Pan, C.-L. Pan, and X.-C. Zhang, "Electrically controlled room temperature terahertz phase shifter with liquid crystal," *IEEE microwave and wireless components letters*, vol. 14, no. 2, pp. 77–79, 2004.
76. X.-w. Lin, J.-b. Wu, W. Hu, Z.-g. Zheng, Z.-j. Wu, G. Zhu, F. Xu, B.-b. Jin, and Y.-q. Lu, "Self-polarizing terahertz liquid crystal phase shifter," *Aip Advances*, vol. 1, no. 3, p. 032133, 2011.
77. K. Altmann, M. Reuter, K. Garbat, M. Koch, R. Dabrowski, and I. Dierking, "Polymer stabilized liquid crystal phase shifter for terahertz waves," *Optics express*, vol. 21, no. 10, pp. 12395–12400, 2013.
78. Y. Wu, X. Ruan, C.-H. Chen, Y. J. Shin, Y. Lee, J. Niu, J. Liu, Y. Chen, K.-L. Yang, X. Zhang *et al.*, "Graphene/liquid crystal based terahertz phase shifters," *Optics express*, vol. 21, no. 18, pp. 21395–21402, 2013.
79. C.-S. Yang, C. Kuo, C.-C. Tang, J. Chen, R.-P. Pan, and C.-L. Pan, "Liquid-crystal terahertz quarter-wave plate using chemical-vapor-deposited graphene electrodes," *IEEE Photonics Journal*, vol. 7, no. 6, pp. 1–8, 2015.
80. C.-S. Yang, T.-T. Tang, P.-H. Chen, R.-P. Pan, P. Yu, and C.-L. Pan, "Voltage-controlled liquid-crystal terahertz phase shifter with indium–tin–oxide nanowhiskers as transparent electrodes," *Optics Letters*, vol. 39, no. 8, pp. 2511–2513, 2014.
81. Y. Du, H. Tian, X. Cui, H. Wang, and Z.-X. Zhou, "Electrically tunable liquid crystal terahertz phase shifter driven by transparent polymer electrodes," *Journal of Materials Chemistry C*, vol. 4, no. 19, pp. 4138–4142, 2016.
82. S. Li, J. Wang, H. Tian, L. Li, J. Liu, G. C. Wang, J. Gao, C. Hu, and Z. Zhou, "Super terahertz phase shifter achieving high transmission and large modulation depth," *Optics Letters*, vol. 45, no. 10, pp. 2834–2837, 2020.
83. A. K. Sahoo, C.-S. Yang, C.-L. Yen, H.-C. Lin, Y.-J. Wang, Y.-H. Lin, O. Wada, and C.-L. Pan, "Twisted nematic liquid-crystal-based terahertz phase shifter using pristine pedot: Pss transparent conducting electrodes," *Applied Sciences*, vol. 9, no. 4, p. 761, 2019.

84. Y.-Y. Ji, F. Fan, M. Chen, L. Yang, and S.-J. Chang, "Terahertz artificial birefringence and tunable phase shifter based on dielectric metasurface with compound lattice," *Optics express*, vol. 25, no. 10, pp. 11405–11413, 2017.
85. B. Scherger, M. Reuter, M. Scheller, K. Altmann, N. Vieweg, R. Dabrowski, J. A. Deibel, and M. Koch, "Discrete terahertz beam steering with an electrically controlled liquid crystal device," *Journal of Infrared, Millimeter, and Terahertz Waves*, vol. 33, no. 11, pp. 1117–1122, 2012.
86. U. Shah, E. Decrossas, C. Jung-Kubiak, T. Reck, G. Chattopadhyay, I. Mehdi, and J. Oberhammer, "Submillimeter-wave 3.3-bit RF MEMS phase shifter integrated in micromachined waveguide," *IEEE Transactions on Terahertz Science and Technology*, vol. 6, no. 5, pp. 706–715, 2016.
87. A. A. Ibrahim, H. N. Shaman, and K. Sarabandi, "A sub-THz rectangular waveguide phase shifter using piezoelectric-based tunable artificial magnetic conductor," *IEEE Transactions on Terahertz Science and Technology*, vol. 8, no. 6, pp. 666–680, 2018.
88. S. Rahiminejad, M. Alonso-delPino, T. J. Reck, A. Peralta, R. Lin, C. Jung-Kubiak, and G. Chattopadhyay, "A low-loss silicon MEMS phase shifter operating in the 550-GHz band," *IEEE Transactions on Terahertz Science and Technology*, vol. 11, no. 5, pp. 477–485, 2021.
89. X. Zhao, U. Shah, O. Glubokov, and J. Oberhammer, "Micromachined subterahertz waveguide-integrated phase shifter utilizing supermode propagation," *IEEE Transactions on Microwave Theory and Techniques*, vol. 69, no. 7, pp. 3219–3227, 2021.
90. M. Y. Glyavin, A. G. Luchinin, and G. Y. Golubiatnikov, "Generation of 1.5-kw, 1-THz coherent radiation from a gyrotron with a pulsed magnetic field," *Physical review letters*, vol. 100, no. 1, p. 015101, 2008.
91. M. Alonso-delPino, C. Jung-Kubiak, T. Reck, N. Llombart, and G. Chattopadhyay, "Beam scanning of silicon lens antennas using integrated piezomotors at submillimeter wavelengths," *IEEE Transactions on Terahertz Science and Technology*, vol. 9, no. 1, pp. 47–54, 2018.
92. M. Alonso-delPino, S. Bosma, C. Jung-Kubiak, G. Chattopadhyay, and N. Llombart, "Wideband multimode leaky-wave feed for scanning lens-phased array at submillimeter wavelengths," *IEEE Transactions on Terahertz Science and Technology*, vol. 11, no. 2, pp. 205–217, 2020.
93. D. Headland, W. Withayachumnankul, R. Yamada, M. Fujita, and T. Nagatsuma, "Terahertz multi-beam antenna using photonic crystal waveguide and luneburg lens," *APL Photonics*, vol. 3, no. 12, p. 126105, 2018.
94. Y. Amarasinghe, R. Mendis, R. Shrestha, H. Guerboukha, J. Taiber, M. Koch, and D. M. Mittleman, "Broadband wide-angle terahertz antenna based on the application of transformation optics to a luneburg lens," *Scientific Reports*, vol. 11, no. 1, pp. 1–8, 2021.
95. K. Sato and Y. Monnai, "Terahertz beam steering based on trajectory deflection in dielectric-free luneburg lens," *IEEE Transactions on Terahertz Science and Technology*, vol. 10, no. 3, pp. 229–236, 2020.
96. R. K. Luneburg, *Mathematical theory of optics*. University of California press, 1964.
97. Y. Amarasinghe, D. M. Mittleman, and R. Mendis, "A luneburg lens for the terahertz region," *Journal of Infrared, Millimeter, and Terahertz Waves*, vol. 40, no. 11, pp. 1129–1136, 2019.
98. W. L. Chan, H.-T. Chen, A. J. Taylor, I. Brener, M. J. Cich, and D. M. Mittleman, "A spatial light modulator for terahertz beams," *Applied Physics Letters*, vol. 94, no. 21, p. 213511, 2009.
99. S. Busch, B. Scherger, M. Scheller, and M. Koch, "Optically controlled terahertz beam steering and imaging," *Optics letters*, vol. 37, no. 8, pp. 1391–1393, 2012.
100. M. I. B. Shams, Z. Jiang, S. M. Rahman, L.-J. Cheng, J. L. Hesler, P. Fay, and L. Liu, "A 740-GHz dynamic two-dimensional beam-steering and forming antenna based on photo-induced reconfigurable fresnel zone plates," *IEEE Transactions on Terahertz Science and Technology*, vol. 7, no. 3, pp. 310–319, 2017.
101. Y. Monnai, K. Altmann, C. Jansen, H. Hillmer, M. Koch, and H. Shinoda, "Terahertz beam steering and variable focusing using programmable diffraction gratings," *Optics express*, vol. 21, no. 2, pp. 2347–2354, 2013.
102. L. Schmitt, X. Liu, A. Czylwik, and M. Hoffmann, "Design and fabrication of MEMS reflectors for THz reflect-arrays," in *2021 Fourth International Workshop on Mobile Terahertz Systems (IWMTS)*. IEEE, 2021, pp. 1–5.
103. C.-J. Lin, C.-H. Lin, Y.-T. Li, R.-P. Pan, and C.-L. Pan, "Electrically controlled liquid crystal phase grating for terahertz waves," *IEEE Photonics Technology Letters*, vol. 21, no. 11, pp. 730–732, 2009.

104. T. P. Steinbusch, H. K. Tyagi, M. C. Schaafsma, G. Georgiou, and J. G. Rivas, "Active terahertz beam steering by photo-generated graded index gratings in thin semiconductor films," *Optics express*, vol. 22, no. 22, pp. 26559–26571, 2014.
105. M. C. Wu, "Micromachining for optical and optoelectronic systems," *Proceedings of the IEEE*, vol. 85, no. 11, pp. 1833–1856, 1997.
106. J. M. Seifert, G. G. Hernandez-Cardoso, M. Koch, and E. Castro-Camus, "Terahertz beam steering using active diffraction grating fabricated by 3D printing," *Optics Express*, vol. 28, no. 15, pp. 21737–21744, 2020.
107. L. Schmitt, P. Schmitt, X. Liu, A. Czylwik, and M. Hoffmann, "Micromechanical reflect-array for THz radar beam steering based on a mechanical d/a converter and a mechanical amplifier," in *2020 Third International Workshop on Mobile Terahertz Systems (IWMTS)*. IEEE, 2020, pp. 1–5.
108. X. Liu, L. Samfaß, K. Kolpatzeck, L. Häring, J. C. Balzer, M. Hoffmann, and A. Czylwik, "Terahertz beam steering concept based on a mems-reconfigurable reflection grating," *Sensors*, vol. 20, no. 10, p. 2874, 2020.
109. L. Schmitt, P. Schmitt, and M. Hoffmann, "3-bit digital-to-analog converter with mechanical amplifier for binary encoded large displacements," in *Actuators*, vol. 10, no. 8. Multidisciplinary Digital Publishing Institute, 2021, p. 182.
110. X. Liu, L. Schmitt, B. Sievert, J. Lipka, C. Geng, K. Kolpatzeck, D. Erni, A. Rennings, J. C. Balzer, M. Hoffmann *et al.*, "Terahertz beam steering using a mems-based reflectarray configured by a genetic algorithm," *IEEE Access*, vol. 10, pp. 84458–84472, 2022.
111. J. Cheng, X. Dong, S. Chen, Y. Yuan, Q. Wen, and S. Chang, "Terahertz metagrating accordion for dynamic beam steering," *Advanced Optical Materials*, p. 2200008, 2022.
112. D. Sievenpiper, J. Schaffner, H. Song, R. Loo, and G. Tangonan, "Two-dimensional beam steering using an electrically tunable impedance surface," *IEEE Transactions on Antennas and Propagation*, vol. 51, no. 10, pp. 2713–2722, 2003.
113. Y. Monnai and H. Shinoda, "Focus-scanning leaky-wave antenna with electronically pattern-tunable scatterers," *IEEE transactions on antennas and propagation*, vol. 59, no. 6, pp. 2070–2077, 2011.
114. L. Li, T. Jun Cui, W. Ji, S. Liu, J. Ding, X. Wan, Y. Bo Li, M. Jiang, C.-W. Qiu, and S. Zhang, "Electromagnetic reprogrammable coding-metasurface holograms," *Nature communications*, vol. 8, no. 1, pp. 1–7, 2017.
115. K. Zhang, H. Yu, X. Ding, and Q. Wu, "Experimental validation of active holographic metasurface for electrically beam steering," *Optics express*, vol. 26, no. 5, pp. 6316–6324, 2018.
116. H.-T. Chen, W. J. Padilla, J. M. Zide, A. C. Gossard, A. J. Taylor, and R. D. Averitt, "Active terahertz metamaterial devices," *Nature*, vol. 444, no. 7119, pp. 597–600, 2006.
117. S. Venkatesh, X. Lu, H. Saeidi, and K. Sengupta, "A high-speed programmable and scalable terahertz holographic metasurface based on tiled CMOS chips," *Nature Electronics*, vol. 3, no. 12, pp. 785–793, 2020.
118. S. Venkatesh, X. Lu, H. Saeidi, and K. Sengupta, "A programmable terahertz metasurface with circuit-coupled meta-elements in silicon chips: Creating low-cost, large-scale, reconfigurable terahertz metasurfaces." *IEEE Antennas and Propagation Magazine*, 2022.
119. Y. Liu, T. Sun, Y. Xu, X. Wu, Z. Bai, Y. Sun, H. Li, H. Zhang, K. Chen, C. Ruan *et al.*, "Active tunable THz metamaterial array implemented in CMOS technology," *Journal of physics D: applied physics*, vol. 54, no. 8, p. 085107, 2020.
120. Y. Zhang, Y. Zhao, S. Liang, B. Zhang, L. Wang, T. Zhou, W. Kou, F. Lan, H. Zeng, J. Han *et al.*, "Large phase modulation of THz wave via an enhanced resonant active hemt metasurface," *Nanophotonics*, vol. 8, no. 1, pp. 153–170, 2019.
121. B. Vasić, G. Isić, R. Beccherelli, and D. C. Zografopoulos, "Tunable beam steering at terahertz frequencies using reconfigurable metasurfaces coupled with liquid crystals," *IEEE Journal of Selected Topics in Quantum Electronics*, vol. 26, no. 5, pp. 1–9, 2019.
122. E. Carrasco, M. Tamagnone, and J. Perruisseau-Carrier, "Tunable graphene reflective cells for THz reflectarrays and generalized law of reflection," *Applied Physics Letters*, vol. 102, no. 10, p. 104103, 2013.
123. B. Sensale-Rodriguez, S. Rafique, R. Yan, M. Zhu, V. Protasenko, D. Jena, L. Liu, and H. G. Xing, "Terahertz imaging employing graphene modulator arrays," *Optics express*, vol. 21, no. 2, pp. 2324–2330, 2013.

124. Y. Malevich, M. S. Ergoktas, G. Bakan, P. Steiner, and C. Kocabas, "Video-speed graphene modulator arrays for terahertz imaging applications," *ACS Photonics*, vol. 7, no. 9, pp. 2374–2380, 2020.
125. C. Wang, Y. Yao, J. Yu, and X. Chen, "3d beam reconfigurable thz antenna with graphene-based high-impedance surface," *Electronics*, vol. 8, no. 11, p. 1291, 2019.
126. H. Ai, Q. Kang, W. Wang, K. Guo, and Z. Guo, "Multi-beam steering for 6g communications based on graphene metasurfaces," *Sensors*, vol. 21, no. 14, p. 4784, 2021.
127. F. Zhao, J. Xu, and Z. Song, "Terahertz multiple beam steering using graphene pancharatnam-berry metasurfaces," *IEEE Photonics Journal*, 2022.
128. Y. Wang, D. Cui, Y. Wang, G. Yang, B. Zhang, Y. Zhang, and C. Wang, "All-solid-state terahertz phased array based on graphene metasurface for ultra-wide-angle beam steering," *Journal of Lightwave Technology*, 2022.
129. S. Savo, D. Shrekenhamer, and W. J. Padilla, "Liquid crystal metamaterial absorber spatial light modulator for THz applications," *Advanced optical materials*, vol. 2, no. 3, pp. 275–279, 2014.
130. J. Wu, Z. Shen, S. Ge, B. Chen, Z. Shen, T. Wang, C. Zhang, W. Hu, K. Fan, W. Padilla *et al.*, "Liquid crystal programmable metasurface for terahertz beam steering," *Applied physics letters*, vol. 116, no. 13, p. 131104, 2020.
131. C. X. Liu, F. Yang, X. J. Fu, J. W. Wu, L. Zhang, J. Yang, and T. J. Cui, "Programmable manipulations of terahertz beams by transmissive digital coding metasurfaces based on liquid crystals," *Advanced Optical Materials*, vol. 9, no. 22, p. 2100932, 2021.
132. M. Jiang, F. Hu, L. Zhang, B. Quan, W. Xu, H. Du, D. Xie, and Y. Chen, "Electrically triggered vo¡sub¿2¡/sub¿ reconfigurable metasurface for amplitude and phase modulation of terahertz wave," *Journal of Lightwave Technology*, vol. 39, no. 11, pp. 3488–3494, 2021.
133. M. R. M. Hashemi, S.-H. Yang, T. Wang, N. Sepúlveda, and M. Jarrahi, "Electronically-controlled beam-steering through vanadium dioxide metasurfaces," *Scientific reports*, vol. 6, no. 1, pp. 1–8, 2016.
134. L. Cong and R. Singh, "Spatiotemporal dielectric metasurfaces for unidirectional propagation and reconfigurable steering of terahertz beams," *Advanced Materials*, vol. 32, no. 28, p. 2001418, 2020.
135. J. Kappa, D. Sokoluk, S. Klingel, C. Shemelya, E. Oesterschulze, and M. Rahm, "Electrically reconfigurable micromirror array for direct spatial light modulation of terahertz waves over a bandwidth wider than 1 THz," *Scientific reports*, vol. 9, no. 1, pp. 1–9, 2019.
136. M. Manjappa, P. Pitchappa, N. Singh, N. Wang, N. I. Zheludev, C. Lee, and R. Singh, "Reconfigurable MEMS fano metasurfaces with multiple-input–output states for logic operations at terahertz frequencies," *Nature communications*, vol. 9, no. 1, pp. 1–10, 2018.
137. T. Niu, W. Withayachumnankul, B. S.-Y. Ung, H. Menekse, M. Bhaskaran, S. Sriram, and C. Fumeaux, "Experimental demonstration of reflectarray antennas at terahertz frequencies," *Optics express*, vol. 21, no. 3, pp. 2875–2889, 2013.
138. S. Li, C. Li, X. Zhang, and G. Fang, "A planar binary structure for realizing frequency controlled beam-steering at 0.2-terahertz band," *IEEE Antennas and Wireless Propagation Letters*, vol. 13, pp. 1007–1010, 2014.
139. S. Li, C. Li, X. Zhang, and G. Fang, "Achievement of beam steering in terahertz band based on frequency-scanning grating-reflector antenna," *Electronics letters*, vol. 50, no. 3, pp. 136–138, 2014.
140. S. Zheng, C. Li, S. Wu, H. Li, G. Yang, and G. Fang, "Terahertz transmissive metasurface for realizing beam steering by frequency scanning," *Journal of Lightwave Technology*, vol. 39, no. 17, pp. 5502–5507, 2021.
141. H. Yi, S.-W. Qu, K.-B. Ng, C. H. Chan, and X. Bai, "3-d printed millimeter-wave and terahertz lenses with fixed and frequency scanned beam," *IEEE Transactions on Antennas and Propagation*, vol. 64, no. 2, pp. 442–449, 2015.
142. R. Camblor, S. Ver Hoeye, M. Fernandez, C. V. Antuña, and F. Las-Heras, "Full 2-d submillimeter-wave frequency scanning array," *IEEE Transactions on Antennas and Propagation*, vol. 65, no. 9, pp. 4486–4494, 2017.
143. K. Murano, I. Watanabe, A. Kasamatsu, S. Suzuki, M. Asada, W. Withayachumnankul, T. Tanaka, and Y. Monnai, "Low-profile terahertz radar based on broadband leaky-wave beam steering," *IEEE Transactions on Terahertz Science and Technology*, vol. 7, no. 1, pp. 60–69, 2016.
144. P. Lu, T. Haddad, B. Sievert, B. Khani, S. Makhlouf, S. Dülme, J. F. Estévez, A. Rennings, D. Erni, U. Pfeiffer *et al.*, "Inp-based THz beam steering leaky-wave antenna," *IEEE Transactions on Terahertz Science and Technology*, vol. 11, no. 2, pp. 218–230, 2020.

145. A. Yariv and M. Nakamura, "Periodic structures for integrated optics," *IEEE journal of quantum electronics*, vol. 13, no. 4, pp. 233–253, 1977.
146. P. Lu, T. Haddad, J. Tebart, M. Steeg, B. Sievert, J. Lackmann, A. Rennings, and A. Stöhr, "Mobile THz communications using photonic assisted beam steering leaky-wave antennas," *Optics Express*, vol. 29, no. 14, pp. 21629–21638, 2021.
147. Y. Monnai, V. Viereck, H. Hillmer, K. Altmann, C. Jansen, M. Koch, and H. Shinoda, "Terahertz beam steering using structured MEMS surfaces for networked wireless sensing," in *2012 Ninth International Conference on Networked Sensing (INSS)*. IEEE, 2012, pp. 1–3.
148. M. Esquius-Morote, J. S. Gómez-Dı, J. Perruisseau-Carrier *et al.*, "Sinusoidally modulated graphene leaky-wave antenna for electronic beamscanning at THz," *IEEE Transactions on Terahertz Science and Technology*, vol. 4, no. 1, pp. 116–122, 2014.
149. W. Fuscaldo, P. Burghignoli, P. Baccarelli, and A. Galli, "A reconfigurable substrate–superstrate graphene-based leaky-wave THz antenna," *IEEE Antennas and Wireless Propagation Letters*, vol. 15, pp. 1545–1548, 2016.
150. Y. Cheng, L.-S. Wu, M. Tang, Y.-P. Zhang, and J.-F. Mao, "A sinusoidally-modulated leaky-wave antenna with gapped graphene ribbons," *IEEE Antennas and Wireless Propagation Letters*, vol. 16, pp. 3000–3004, 2017.
151. J. Li, M. He, C. Wu, and C. Zhang, "Radiation-pattern-reconfigurable graphene leaky-wave antenna at terahertz band based on dielectric grating structure," *IEEE Antennas and Wireless Propagation Letters*, vol. 16, pp. 1771–1775, 2017.
152. M. Gao, K. Li, F. Kong, H. Zhuang, and G. Zhu, "Graphene-based composite right/left-handed leaky-wave antenna at terahertz," *Plasmonics*, vol. 15, no. 4, pp. 1199–1204, 2020.
153. M. Gao, K. Li, F. Kong, G. Zhu, S. Wang, and H. Zhuang, "Terahertz quasi-tem mode tunable composite right/left-handed leaky-wave antennas using graphene-based coplanar waveguides," *Plasmonics*, vol. 16, no. 4, pp. 1151–1164, 2021.
154. H. Soleimani and H. Oraizi, "Plasmonic leaky wave antenna based on modulated radius of cylindrical graphene waveguide," *AIP Advances*, vol. 11, no. 9, p. 095318, 2021.
155. A. Gomez-Torrent, M. Garcia-Vigueras, L. Le Coq, A. Mahmoud, M. Ettorre, R. Sauleau, and J. Oberhammer, "A low-profile and high-gain frequency beam steering subterahertz antenna enabled by silicon micromachining," *IEEE Transactions on Antennas and Propagation*, vol. 68, no. 2, pp. 672–682, 2019.
156. N. J. Karl, R. W. McKinney, Y. Monnai, R. Mendis, and D. M. Mittleman, "Frequency-division multiplexing in the terahertz range using a leaky-wave antenna," *Nature Photonics*, vol. 9, no. 11, pp. 717–720, 2015.
157. B. Beuerle, J. Campion, U. Shah, and J. Oberhammer, "A very low loss 220–325 GHz silicon micromachined waveguide technology," *IEEE Transactions on Terahertz science and technology*, vol. 8, no. 2, pp. 248–250, 2018.
158. Y.-W. Wu, Z. Jiang, and Z.-C. Hao, "A 400-GHz low cost planar leaky-wave antenna with low sidelobe level and low cross-polarization level," *IEEE Transactions on Terahertz Science and Technology*, vol. 10, no. 4, pp. 427–430, 2020.
159. K. Sarabandi, A. Jam, M. Vahidpour, and J. East, "A novel frequency beam-steering antenna array for submillimeter-wave applications," *IEEE Transactions on Terahertz Science and Technology*, vol. 8, no. 6, pp. 654–665, 2018.
160. H. Guerboukha, R. Shrestha, J. Neronha, O. Ryan, M. Hornbuckle, Z. Fang, and D. Mittleman, "Efficient leaky-wave antennas at terahertz frequencies generating highly directional beams," *Applied Physics Letters*, vol. 117, no. 26, p. 261103, 2020.
161. D. R. Jackson, C. Caloz, and T. Itoh, "Leaky-wave antennas," *Proceedings of the IEEE*, vol. 100, no. 7, pp. 2194–2206, 2012.
162. A. A. Tavallaee, B. S. Williams, P. W. Hon, T. Itoh, and Q.-S. Chen, "Terahertz quantum-cascade laser with active leaky-wave antenna," *Applied Physics Letters*, vol. 99, no. 14, p. 141115, 2011.
163. R. Camblor, S. Ver Hoeye, M. Fernandez, C. V. Antuña, and F. Las-Heras, "Submillimeter wavelength 2-d frequency scanning antenna based on slotted waveguides fed through a phase shifting network," *IEEE Transactions On Antennas And Propagation*, vol. 65, no. 7, pp. 3501–3509, 2017.
164. S. S. Yao, Y. J. Cheng, Y. F. Wu, and H. N. Yang, "Thz 2-d frequency scanning planar integrated array antenna with improved efficiency," *IEEE Antennas and Wireless Propagation Letters*, vol. 20, no. 6, pp. 983–987, 2021.

165. K. Sato and Y. Monnai, "Two-dimensional terahertz beam steering based on trajectory deflection of leaky-mode," *IEEE Transactions on Terahertz Science and Technology*, vol. 11, no. 6, pp. 676–683, 2021.
166. H. Saeidi, S. Venkatesh, X. Lu, and K. Sengupta, "THz prism: One-shot simultaneous localization of multiple wireless nodes with leaky-wave THz antennas and transceivers in CMOS," *IEEE Journal of Solid-State Circuits*, vol. 56, no. 12, pp. 3840–3854, 2021.
167. H. Hassanieh, O. Abari, M. Rodriguez, M. Abdelghany, D. Katabi, and P. Indyk, "Fast millimeter wave beam alignment," in *Proceedings of the 2018 Conference of the ACM Special Interest Group on Data Communication*, 2018, pp. 432–445.
168. M. Pengnoo, M. T. Barros, L. Wuttisittikulkij, B. Butler, A. Davy, and S. Balasubramaniam, "Digital twin for metasurface reflector management in 6g terahertz communications," *IEEE access*, vol. 8, pp. 114580–114596, 2020.
169. H. Saeidi, S. Venkatesh, X. Lu, and K. Sengupta, "22.1 thz prism: one-shot simultaneous multi-node angular localization using spectrum-to-space mapping with 360-to-400ghz broadband transceiver and dual-port integrated leaky-wave antennas," in *2021 IEEE International Solid-State Circuits Conference (ISSCC)*, vol. 64. IEEE, 2021, pp. 314–316.
170. J. Ma, N. J. Karl, S. Bretin, G. Ducournau, and D. M. Mittleman, "Frequency-division multiplexer and demultiplexer for terahertz wireless links," *Nature communications*, vol. 8, no. 1, pp. 1–8, 2017.
171. Y. Ghasempour, R. Shrestha, A. Charous, E. Knightly, and D. M. Mittleman, "Single-shot link discovery for terahertz wireless networks," *Nature communications*, vol. 11, no. 1, pp. 1–6, 2020.
172. H. Matsumoto, I. Watanabe, A. Kasamatsu, and Y. Monnai, "Integrated terahertz radar based on leaky-wave coherence tomography," *Nature Electronics*, vol. 3, no. 2, pp. 122–129, 2020.
173. D. M. Mittleman, "Twenty years of terahertz imaging," *Optics express*, vol. 26, no. 8, pp. 9417–9431, 2018.
174. S. Schumann, C. Jansen, M. Schwerdtfeger, S. Busch, O. Peters, M. Scheller, and M. Koch, "Spectrum to space transformed fast terahertz imaging," *Optics express*, vol. 20, no. 17, pp. 19200–19205, 2012.
175. S. Li, C. Li, W. Liu, Z. Sun, S. Lang, Z. Lu, X. Zhang, and G. Fang, "Study of terahertz super-resolution imaging scheme with real-time capability based on frequency scanning antenna," *IEEE Transactions on Terahertz Science and Technology*, vol. 6, no. 3, pp. 451–463, 2016.
176. K. Murata, K. Murano, I. Watanabe, A. Kasamatsu, T. Tanaka, and Y. Monnai, "See-through detection and 3D reconstruction using terahertz leaky-wave radar based on sparse signal processing," *Journal of Infrared, Millimeter, and Terahertz Waves*, vol. 39, no. 2, pp. 210–221, 2018.
177. Y. Amarasinghe, R. Mendis, and D. M. Mittleman, "Real-time object tracking using a leaky THz waveguide," *Optics express*, vol. 28, no. 12, pp. 17997–18005, 2020.
178. X. Chen, M. I. W. Khan, X. Yi, X. Li, W. Chen, J. Zhu, Y. Yang, K. E. Kolodziej, N. M. Monroe, and R. Han, "A 140GHz transceiver with integrated antenna, inherent-low-loss duplexing and adaptive self-interference cancellation for FMCW monostatic radar," in *2022 IEEE International Solid- State Circuits Conference (ISSCC)*, vol. 65, 2022, pp. 80–82.
179. X. Yi, C. Wang, X. Chen, J. Wang, J. Grajal, and R. Han, "A 220-to-320-GHz FMCW radar in 65-nm CMOS using a frequency-comb architecture," *IEEE Journal of Solid-State Circuits*, vol. 56, no. 2, pp. 327–339, 2021.
180. P. Hillger, J. Grzyb, R. Jain, and U. R. Pfeiffer, "Terahertz imaging and sensing applications with silicon-based technologies," *IEEE Transactions on Terahertz Science and Technology*, vol. 9, no. 1, pp. 1–19, 2018.
181. J. Grzyb, K. Statnikov, N. Sarmah, B. Heinemann, and U. R. Pfeiffer, "A 210–270-ghz circularly polarized fmcw radar with a single-lens-coupled sige hbt chip," *IEEE Transactions on Terahertz Science and Technology*, vol. 6, no. 6, pp. 771–783, 2016.
182. S. M. Hossein Naghavi, S. Seyedabbaszadehesfahlani, F. Khoeini, A. Cathelin, and E. Afshari, "22.4 a 250GHz autodyne FMCW radar in 55nm biCMOS with micrometer range resolution," in *2021 IEEE International Solid- State Circuits Conference (ISSCC)*, vol. 64, 2021, pp. 320–322.
183. D. Simic, K. Guo, and P. Reynaert, "22.3 a 0.42THz coherent tx-rx system achieving 10dBm EIRP and 27db nf in 40nm CMOS for phase-contrast imaging," in *2021 IEEE International Solid- State Circuits Conference (ISSCC)*, vol. 64, 2021, pp. 318–320.
184. G. H. Knittel, A. Hessel, and A. A. Oliner, "Element pattern nulls in phased arrays and their relation to guided waves," *Proceedings of the IEEE*, vol. 56, no. 11, pp. 1822–1836, 1968.

185. D. Pozar and D. Schaubert, "Scan blindness in infinite phased arrays of printed dipoles," *IEEE Transactions on Antennas and Propagation*, vol. 32, no. 6, pp. 602–610, 1984.
186. Y. Fu and N. Yuan, "Elimination of scan blindness in phased array of microstrip patches using electromagnetic bandgap materials," *IEEE Antennas and Wireless Propagation Letters*, vol. 3, pp. 63–65, 2004.
187. L. Zhang, J. A. Castaneda, and N. G. Alexopoulos, "Scan blindness free phased array design using pbg materials," *IEEE Transactions on Antennas and Propagation*, vol. 52, no. 8, pp. 2000–2007, 2004.
188. X. Liang, Z. Zhang, J. Zeng, F. Guan, X. Liu, and J. Zi, "Scan blindness free design of wideband wide-scanning open-ended waveguide phased array," *IEEE Access*, vol. 9, pp. 68127–68138, 2021.
189. K. K. W. Low, S. Zihir, T. Kanar, and G. M. Rebeiz, "A 27-31-GHz 1024-element ka-band satcom phased-array transmitter with 49.5-dbw peak EIRP, 1-db ar, and$\pm 70^\circ$ beam scanning," *IEEE Transactions on Microwave Theory and Techniques*, 2022.
190. S. M. Bowers, A. Safaripour, and A. Hajimiri, "Dynamic polarization control," *IEEE Journal of Solid-State Circuits*, vol. 50, no. 5, pp. 1224–1236, 2015.
191. A. Safaripour, S. M. Bowers, K. Dasgupta, and A. Hajimiri, "Dynamic polarization control of two-dimensional integrated phased arrays," *IEEE Transactions on Microwave Theory and Techniques*, vol. 64, no. 4, pp. 1066–1077, 2016.
192. K. Sasao and Y. Monnai, "Voltage-controlled polarization at 0.1 thz based on phase-tuned coupled oscillation via a magic tee," *IEEE Transactions on Terahertz Science and Technology*, vol. 12, no. 6, pp. 587–591, 2022.
193. S. Venkatesh, X. Lu, B. Tang, and K. Sengupta, "Secure space–time-modulated millimetre-wave wireless links that are resilient to distributed eavesdropper attacks," *Nature Electronics*, vol. 4, no. 11, pp. 827–836, 2021.
194. Z. Yu, X. Lu, C. Gu, S. Venkatesh, and J. Mao, "mmwave spatial-temporal single harmonic switching transmitter arrays for high back-off beamforming efficiency," *IEEE Transactions on Antennas and Propagation*, pp. 1–1, 2022.
195. X. Lu, S. Venkatesh, B. Tang, and K. Sengupta, "4.6 space-time modulated 71-to-76ghz mm-wave transmitter array for physically secure directional wireless links," in *2020 IEEE International Solid-State Circuits Conference-(ISSCC)*. IEEE, 2020, pp. 86–88.
196. J. S. Jensen and O. Sigmund, "Topology optimization for nano-photonics," *Laser & Photonics Reviews*, vol. 5, no. 2, pp. 308–321, 2011.
197. S. Molesky, Z. Lin, A. Y. Piggott, W. Jin, J. Vucković, and A. W. Rodriguez, "Inverse design in nanophotonics," *Nature Photonics*, vol. 12, no. 11, pp. 659–670, 2018.
198. W. Ma, Z. Liu, Z. A. Kudyshev, A. Boltasseva, W. Cai, and Y. Liu, "Deep learning for the design of photonic structures," *Nature Photonics*, vol. 15, no. 2, pp. 77–90, 2021.
199. Z. Liu, E. A. Karahan, and K. Sengupta, "Deep learning-enabled inverse design of 30–94 ghz p sat, 3db sige pa supporting concurrent multiband operation at multi-gb/s," *IEEE Microwave and Wireless Components Letters*, vol. 32, no. 6, pp. 724–727, 2022.